



**Peer Reviewed**

**Title:**

Hybrid Solar Forecasting Methodologies using Cloud Tracking Techniques and Stochastic Learning Methods

**Author:**

[Chu, Yinghao](#)

**Acceptance Date:**

2015

**Series:**

[UC San Diego Electronic Theses and Dissertations](#)

**Degree:**

Ph. D., [UC San Diego](#)

**Permalink:**

<http://escholarship.org/uc/item/73d4t8j9>

**Local Identifier(s):**

**Abstract:**

Solar forecasts are important for low-cost integration of solar energy into the smart grid. Accurate intra-hour predictions of irradiance quantify the variability of solar power at ground level, reduce the uncertainty in power output from solar farm, and are important for real-time grid balancing and management. A multilayered-hybrid- algorithm method is developed to generate real-time intra-hour prediction intervals (PIs) for both global and direct solar irradiance. This forecasting method integrates stochastic learning methods for the prediction of solar irradiation and local sensing techniques for the introduction of exogenous inputs. The research of the proposed forecasting method consists of four objectives : (1) Development of a smart forecasting engine based on advanced stochastic learning methods. (2) Development of an image-based cloud detection system using a cost- competitive fish-eye camera. (3) Integration of the smart forecasting engine with the cloud detection system to create a high-fidelity forecasting model. (4) Development of a hybrid algorithm to provide prediction intervals for the integrated forecasting model. The forecasting method introduced here is deployed in real-time and achieves forecast skills up to 20% over the reference persistence model. Real-time PIs generated from this method achieve coverage probabilities which are consistently higher than the nominal confidence level (90%) regardless of weather condition

**Copyright Information:**

All rights reserved unless otherwise indicated. Contact the author or original publisher for any necessary permissions. eScholarship is not the copyright owner for deposited works. Learn more at [http://www.escholarship.org/help\\_copyright.html#reuse](http://www.escholarship.org/help_copyright.html#reuse)



eScholarship  
University of California

eScholarship provides open access, scholarly publishing services to the University of California and delivers a dynamic research platform to scholars worldwide.

UNIVERSITY OF CALIFORNIA, SAN DIEGO

**Hybrid Solar Forecasting Methodologies using Cloud Tracking  
Techniques and Stochastic Learning Methods**

A dissertation submitted in partial satisfaction of the requirements for the degree Doctor  
of Philosophy

in

Engineering Sciences (Mechanical Engineering)

by

Yinghao Chu

Committee in charge:

Professor Carlos F. M. Coimbra, Chair  
Professor Jan Kleissl  
Professor Renkun Chen  
Professor Sungho Jin  
Professor Tara Javidi

2015

Copyright

Yinghao Chu, 2015

All rights reserved

The Dissertation of Yinghao Chu is approved, and it is acceptable in quality and form for  
publication on microfilm and electronically:

---

---

---

---

---

Chair

University of California, San Diego

2015

## **DEDICATION**

This work is dedicated to my family – you have always been  
supportive of my endeavors.

## TABLE OF CONTENTS

<b>SIGNATURE PAGE .....</b>	<b>iii</b>
<b>DEDICATION.....</b>	<b>iv</b>
<b>TABLE OF CONTENTS .....</b>	<b>v</b>
<b>LIST OF FIGURES .....</b>	<b>vii</b>
<b>LIST OF TABLES.....</b>	<b>ix</b>
<b>ACKNOWLEDGEMENTS .....</b>	<b>x</b>
<b>VITA.....</b>	<b>xii</b>
<b>ABSTRACT OF THE DISSERTATION.....</b>	<b>xiii</b>
<b>1 Introduction .....</b>	<b>1</b>
<b>2 Background .....</b>	<b>7</b>
2.1 Solar Radiation Measurement .....	7
2.2 Sky Imaging Techniques .....	12
2.3 Stochastic Learning Methods .....	16
2.3.1 Artificial Neural Network .....	16
2.3.2 Validation Methods .....	18
2.3.3 Genetic Algorithm.....	20
2.3.4 Support Vector Machine .....	22
2.4 Assessment of Forecasts .....	23
<b>3 Smart Forecasting Engine .....</b>	<b>26</b>
3.1 Methods .....	26
3.2 Case Study: Power Generation Reforecast from a 48 MWe Photovoltaic Plant .....	28
3.3 Summary .....	37
Acknowledgements .....	38
<b>4 Smart Adaptive Cloud Identification System.....</b>	<b>39</b>

4.1 Fish-eye Camera for Sky Imaging.....	39
4.2 Methods .....	40
4.3 Case Study: SACI Cloud Detection for SkyCam Images .....	44
4.4 Summary .....	49
Acknowledgements .....	50
<b>5 Integrated Smart Forecasting Model .....</b>	<b>51</b>
5.1 Methods .....	51
5.2 Case study: ISFM Using TSI.....	55
5.3 Case Study: ISFM Using SkyCam .....	62
5.4 Summary .....	67
Acknowledgements .....	68
<b>6 Prediction Intervals for ISFM .....</b>	<b>69</b>
6.1 Methods .....	69
6.2 Case Study: Prediction Intervals for Intra-hour DNI Forecast.....	74
6.3 Case Study: Real Time Forecasting.....	80
6.4 Summary .....	86
Acknowledgements .....	88
<b>7 Conclusions and Recommendations for Future Work .....</b>	<b>89</b>
<b>References .....</b>	<b>92</b>

## LIST OF FIGURES

<b>Figure 2.1</b> The components of solar irradiance onto a horizontal surface at ground level: the attenuated direct irradiance and diffuse irradiance. ....	7
<b>Figure 2.2</b> Solar measurement instruments: (a) Eppley thermopile-based precision spectral pyranometer; (b) LI-COR photodiode based pyranometer; (c) Eppley thermopile-based normal incidence pyrliometer mounted on a sun tracker. ....	12
<b>Figure 2.3</b> The sky imaging equipments. (a) Yankee Environmental Systems (YES) Total Sky Imager (Chow et al., 2011); (b) Vivotek FE8171V Vandal-Proof Fish-eye Network Camera. ....	14
<b>Figure 2.4</b> (a) The basic function of a neuron. (b) An example of feed-forward neural network. ....	17
<b>Figure 2.5</b> An example of five-fold cross-validation method. The learning data are divided into five subsets, one of which is reserved for validation and the others are used for training of ANN. ....	19
<b>Figure 2.6</b> a) The iterative activities of the population during generations. b) The illustration of the recombine and mutations.....	21
<b>Figure 3.1</b> The power series used in this case study. 28 days of forecasted data (11/01/11—12/05/11) utilize 26,638 time points. ....	30
<b>Figure 3.2</b> Genetic algorithm identification of the optimal reforecast-ANN topology.....	31
<b>Figure 3.3</b> Plot of testing RMSEs for 5, 10, and 15 minutes horizons. ....	34
<b>Figure 3.4</b> Plots of error ( $\epsilon$ ) Distributions for 10 minutes horizon forecasts. ....	34
<b>Figure 3.5</b> Plots of error ( $\epsilon$ ) Distributions for 15 minutes ahead forecasts. ....	34
<b>Figure 3.6</b> Sample time series of forecasted power generation and absolute forecast errors: (a) deterministic and smart deterministic, (b) ARMA and smart ARMA, and (c) kNN and smart kNN. ....	37
<b>Figure 4.1</b> Framework of smart adaptive cloud identification system (SACI). The dash square encloses the smart adaptive thresholding set (SAT). ....	43
<b>Figure 4.2</b> Representative SACI cloud detection for clear, overcast, partly cloudy with	



optically thick, and optically thin cloud genres sky images. n. ....	47
<b>Figure 5.1</b> Main steps of the cloud tracking method.....	52
<b>Figure 5.2</b> The daily Sun percentage plot for the period from April 28, 2011 to October 30, 2011.....	57
<b>Figure 5.3</b> Plot of daily RMSE of smart forecast against persistent forecast; each marker stands for one testing day. ....	59
<b>Figure 5.4</b> Plot of absolute forecast error against DNI variability for (a) 5 minutes and (b) 10 minutes ahead forecasts. Round markers stand for persistence forecast, triangular markers stand for deterministic forecast, and square markers stand for smart forecast.. ....	61
<b>Figure 5.5</b> Examples of SACI cloud identification for the Folsom SkyCam for (a) clear, (b) overcast, and (c) partly cloudy with optically thick clouds, and (d) optically thin clouds sky images.....	65
<b>Figure 5.6</b> Plots of error distributions for (a) 5 min, (b) 10 min, and (c) 15 min forecasts. ANN <sub>c</sub> represents the ANN-based ISFM forecast using cloud-tracking techniques. The y-axis of the plots is in logarithmic scale.....	67
<b>Figure 6.1</b> Examples of original images (top row) and normalized RBR (NRBR) images (bottom row) for clear period (left column), overcast period (mid column), and partly cloudy (right column) period. The greyscales indicate the NRBR magnitudes in each image.....	70
<b>Figure 6.2</b> (a) Forecast results of persistence, Bootstrap-ANN, and Hybrid models for various forecast horizons in 3-D space. X-axis represents PICP, y-axis represents PINAW, and z-axis represents the confidence level. (b) Plot of PINAWs with respect to PICPs. Each marker stands for one validation result that same to (a). ....	78
<b>Figure 6.3</b> Sample time series of 10-minute horizon PI forecasts for persistence, Bootstrap-ANN, and Hybrid models: a) clear period, b) overcast period, c) and d) partly cloudy period. ....	80
<b>Figure 6.4</b> Sample time series of 10-minute horizon forecasts from the persistence and the Hybrid models: (a) clear period, (b) overcast period, (c) and (d) partly cloudy period. ....	85
<b>Figure 6.5</b> Display of online Real-time forecasting. ....	86

## LIST OF TABLES

<b>Table 3.1</b> Testing results for 5-, 10-, and 15-minutes horizons. The highlighted numbers identify the best performing method for a given metric. ....	30
<b>Table 3.2</b> Statistical results of the analysis for the error distributions. ....	33
<b>Table 4.1</b> Confusion matrix of automatic cloud detection for each pixel. ....	43
<b>Table 4.2</b> Optimal thresholds that maximize the cloud identification accuracy on the learning data set. The third column represents the threshold values used by the methods listed in the second column. ....	46
<b>Table 4.3</b> The results of training accuracy for cloud detection. ....	46
<b>Table 4.4</b> The validation results for Merced, California. ....	46
<b>Table 4.5</b> The validation results for Folsom, California. ....	47
<b>Table 5.1</b> Forecast Performance for the Different Models Applied to the Independent Testing Set as a Function of the Forecasting Horizon. ....	59
<b>Table 5.2</b> Statistical error metrics for testing results of the different forecast models for 5, 10, and 15 minutes horizons. ....	67
<b>Table 6.1</b> Results of CWCs for overall, low variability, and high variability periods on validation set. Boldface font identifies the best performance. ....	77
<b>Table 6.2</b> Classification accuracy of DNI variability level in real time forecasting. ....	82
<b>Table 6.3</b> Results for real-time point forecasts in terms of statistical metrics. MBE, MAE, and RMSE are in ( $\text{W/m}^2$ ). ....	82
<b>Table 6.4</b> Real time results of PICPs, PINAWs, and CWCs. ....	83

## **ACKNOWLEDGEMENTS**

I would like to acknowledge Professor Carlos F. M. Coimbra for his support and advice during the past several years of my research. His guidance is invaluable.

I would also like to acknowledge Dr. Hugo T. C. Pedro, who helped countless times during the past several years of my research.

Chapter 3, in part, is a reprint of the publication: Y. Chu, B. Urquhart, S.M.I. Gohari, H.T.C. Pedro, J. Kleissl and C.F.M. Coimbra (2015) “Short-Term Reforecasting of Power Output from a 48 MWe Solar PV Plant”, *Solar Energy* (112), pp. 68-77. The dissertation author was the first author of this paper.

Chapter 4, in part, is a reprint of the publication: Y. Chu, L. Nonnenmacher, R.H. Inman, Z. Liao, H.T.C. Pedro, and C.F.M. Coimbra (2014) “A Smart Image-Based Cloud Detection System for Intra-Hour Solar Irradiance Forecasts”, *Journal of Atmospheric and Oceanic Technology* (31) pp. 1995-2007. The dissertation author was the first author of this paper.

Chapter 5, in part, is a reprint of the publications: Y. Chu, H.T.C. Pedro, and C.F.M. Coimbra (2013) “Hybrid Intra-Hour DNI Forecasts with Sky Image Processing Enhanced by Stochastic Learning”, *Solar Energy* (98) pp. 592-603; and Y. Chu, H.T.C. Pedro, M. Li, and C.F.M. Coimbra (2015) “Real-Time Forecasting of GHI and DNI Solar Ramps with Smart Image Processing”, *Solar Energy* (114) pp. 91-104. The dissertation author was the first author of these papers.

Chapter 6, in part, is a reprint of the publication: Y. Chu, M. Li, H.T.C. Pedro, and C.F.M. Coimbra (2015) “Real-time Prediction Intervals for Intra-hour DNI Forecasts”, Renewable Energy (in press). The dissertation author was the first author of this paper.

## VITA

2010	Bachelor of Science, Hong Kong University of Science and Technology
2011	Master of Science, University of California, San Diego
2011-2014	Research Assistant, University of California, San Diego
2015	Doctor of Philosophy, University of California, San Diego

## Publications

- Chu, Y., Li, M., Pedro, H.T.C. and Coimbra, C.F.M. (2014) “Real-time Prediction Interval for Intra-hour DNI forecasts”. Renewable Energy (in press).
- Chu, Y., Wang, B., Yang, W., Jung, J., Meyers, M.A., and Coimbra, C.F.M. (2014) “Structure and Mechanical Properties of a Sustainable Substitute for Ivory”. Submitted to Scientific Reports.
- Chu, Y., Li, M., Pedro, H.T.C., and Coimbra, C.F.M. (2014) “Real-Time Forecasting of GHI and DNI Solar Ramps with Smart Image Processing”. Solar Energy (114) pp. 91-104.
- Chu, Y., Urquhart, B., Gohari, S.M.I., Pedro, H.T.C., Kleissl, J., and Coimbra, C.F.M. (2014) “Short-Term Reforecasting of Power Output from a 48 MWe Solar PV Plant”. Solar Energy (112) pp. 68-77.
- Chu, Y., Nonnenmacher, L., Inman, R.H., Liao, Z., Pedro, H.T.C., and Coimbra, C.F.M. (2014) “A Smart Image-Based Cloud Detection System for Intra-Hour Solar Irradiance Forecasts”. AMS Journal of Atmospheric and Oceanic Technology (31) pp. 1996-2008.
- Chu, Y., Pedro, H.T.C., and Coimbra, C.F.M. (2013) “Hybrid Intra-Hour DNI Forecasts with Sky Image Processing Enhanced by Stochastic Learning”. Solar Energy (98) pp. 592-603.

## Field of Study

- Major Field: Engineering Sciences (Solar Energy Forecast and Integration)
- Local Sensing and Image Processing Techniques
- Sustainable Biological Material

## **ABSTRACT OF THE DISSERTATION**

Hybrid Solar Forecasting Methodologies using Cloud Tracking Techniques and  
Stochastic Learning Methods

by

Yinghao Chu

Doctor of Philosophy in Engineering Sciences (Mechanical Engineering)

University of California, San Diego, 2015

Professor Carlos F. M. Coimbra, Chair

Solar forecasts are important for low-cost integration of solar energy into the smart grid. Accurate intra-hour predictions of irradiance quantify the variability of solar power at ground level, reduce the uncertainty in power output from solar farm, and are important for real-time grid balancing and management.

A multilayered-hybrid-algorithm method is developed to generate real-time intra-hour prediction intervals (PIs) for both global and direct solar irradiance. This

forecasting method integrates stochastic learning methods for the prediction of solar irradiation and local sensing techniques for the introduction of exogenous inputs.

The research of the proposed forecasting method consists of four objectives: (1) Development of a smart forecasting engine based on advanced stochastic learning methods. (2) Development of an image-based cloud detection system using a cost-competitive fish-eye camera. (3) Integration of the smart forecasting engine with the cloud detection system to create a high-fidelity forecasting model. (4) Development of a hybrid algorithm to provide prediction intervals for the integrated forecasting model.

The forecasting method introduced here is deployed in real-time and achieves forecast skills up to 20% over the reference persistence model. Real-time PIs generated from this method achieve coverage probabilities which are consistently higher than the nominal confidence level (90%) regardless of weather conditions.

# 1 Introduction

The global consumption of energy is expected to continually increase (Singh (2013)). Traditional fossil fuels still dominate the global energy productions and raise serious concerns about their environmental impacts. Therefore, the urgency to find sustainable sources of energy has motivated the rapid growth of solar energy productions. Progressive energy policies in California require that 33% of the state's energy production originate from renewable sources by the year 2020, and the state of California is responsible for 47% of all solar installations in US (CAISO (2010), NREL (2010)). Solar power technologies are functionally ready and nearly financially competitive to be deployed at grid scale. However, the variable and intermittent nature of the solar resource remains a major obstacle to achieving higher levels of grid penetration (Mellit & Kalogirou (2008), Paoli et al. (2010)). The electric power grid needs to be balanced in real-time, and storage and spinning reserves are generally limited. At increasingly high level of solar penetration, sudden power drops caused by atmospheric processes result in instantaneous fluctuations in the solar power production and adversely affect grid stability. With the growing demands for solar generation and integration, the development of solar forecasting tools to mitigate the solar uncertainty is of critical importance (CAISO (2010)).

With the assistance of accurate forecasts, fluctuations of irradiance and power generation can be anticipated. Therefore, smart DC/AC inverters can respond in time to



power generation ramps, the utility companies can know in advance how much supplementary energy must be generated to balance grid, and grid operators can make informed operating decisions to maintain the stability of grid. Accurate solar forecasting is an essential component of a smarter, more dynamic power grid that is capable of absorbing increasingly higher levels of intermittent renewable resources.

The simplest forecast model for short-term horizons is the persistence model, which works well for periods of low solar irradiance variability (consistently clear or consistently overcast days) and is still widely used as a reference model. However, the accuracy of the persistence model is reduced substantially when irradiance variability increases. Statistically, persistence modeling misses all important ramps that are more likely to cause grid integration issues. Accurate forecasts of irradiance and power ramps, which occur mostly during periods of high irradiance variability, are essential to grid balancing.

Data-driven models based on the analysis of historical time series, such as the auto-regressive and stochastic-learning models, have been developed and outperform the persistent model. Among these models, Artificial Neural Networks (ANNs) are some of the widely used methods (Elizonodo et al. (1994), Cao & Lin (2008), Martin et al. (2010), Mellit & Pavan (2010), Mellit et al. (2010), Marquez & Coimbra (2011), Inman et al. (2013)). Nevertheless, most of these data-driven models do not consider the

spatial-temporal information of clouds, which are known to be one of the dominant factors affecting ground irradiance levels (Chu et al. 2014).

Some models incorporate sky cover information using remote sensing techniques (Hammer et al. (1999), Perez et al. (2010), Marquez et al. (2013)). However, the temporal resolution (>30 minutes) and the spatial resolution (>1 kilometer) of satellite images are inappropriate for intra-hour solar forecasts. In order to overcome this issue, high-frequency image-capturing devices, such as Total Sky Imagers (TSIs), are used to capture local sky images and extract cloud cover information (Crispim et al. (2008), Chow et al. (2011), Marquez & Coimbra (2012)). For example, Marquez and Coimbra (2012) describe a deterministic DNI forecasting model based on TSI images. This model achieves lower RMSEs than the persistence model on a few selected days for 3- to 15-minute forecast horizons. However, commercial sky imagers are costly and incorporate shading systems that reduce the ability of tracking circumsolar clouds. In addition, these sky-imaging based models do not involve stochastic learning methodologies to further improve the accuracy of forecasts.

Both stochastic learning methods and cloud tracking methods are widely used for solar forecasts. However, very few studies integrate these two methods, particularly for intra-hour solar forecasts. In addition, most of the solar forecasting models make point or time average predictions without considering the forecast uncertainty. In practice, there are inherent and irreducible forecasting errors associated with point forecasts regardless

of the data processing, the mechanism of model, the explanatory variables, and the model training methods (Khosravi et al. (2013)):

$$T(t) = f(t) + \varepsilon(t), \quad (1)$$

where  $T(t)$  is the measured (target) value at time  $t$ ,  $f(t)$  is the true regression, and  $\varepsilon(t)$  is the unbiased noise. Prediction Intervals (PIs), in which target values  $T$  will fall with a probability, quantify the uncertainty in predicting the target values  $T(t)$ , and therefore are more useful than point predictions for decision-making in real-world applications (Carney et al. (1999), Pinson et al. (2007), Khosravi et al. (2013)).

To address all the mentioned drawbacks of available forecasts, a Hybrid, multilayered Integrated Solar Forecasting Model (denoted as Hybrid-ISFM) is developed to generate the real-time PIs of one-minute averaged irradiance for intra-hour forecasting horizons (ranging from 5 to 20 minutes). This Hybrid-ISFM, which integrates inexpensive local sensing techniques and advanced stochastic learning methods, is developed using high-quality irradiance and imaging measurements recorded at multiple locations in California.

The development of the Hybrid-ISFM includes four major steps: First, a smart forecasting engine is developed based on a multilayer perceptron, whose scheme will be optimized using Genetic Algorithms (GA). This system is validated and optimized by measured irradiance and power data. Subsequently, a new local-sensing system based on off-the-shelf fish-eye sky cameras is developed. This new system is expected to be

superior to the current TSI imaging system in several aspects: cost efficiency, spatial resolution, portability and convenient installation. Thirdly, the optimized smart forecasting engine is integrated with the new cloud-tracking system to develop an integrated solar forecast model (ISFM). The ISFM is validated using measured meteorological data from our observatories in multiple locations. Eventually, a Hybrid model, which integrates Support Vector Machine (SVM) and Artificial Neural Networks (ANN), is developed to quantify the forecast uncertainties and to provide PIs for the ISFM. The combination of the Hybrid model and the ISFM is denoted as the Hybrid-ISFM, which is deployed in real time to generate PIs. Three performance metrics (introduced in Chapter 2) are used to assess the real-time PIs under diverse weather conditions.

This dissertation is organized as followed: Chapter 2 presents the necessary background information of this study, including solar radiation measurements, sky imaging techniques, stochastic learning methods, and metrics used to assess the performance of the forecasts. Chapter 3 presents the development of the smart forecasting engine. Chapter 4 presents the development of the sky camera-based cloud-detection system. Chapter 5 presents the development and the performance of the integrated solar forecasting model (ISFM) for our multiple observatories in California. Chapter 6 presents the development of the Hybrid-ISFP. This chapter also presents the real-time performance of the Hybrid-ISFM when deployed as a proof-of-concept at an observatory located in

Folsom, CA. Conclusion and future works are presented in the Chapter 7.

## 2 Background

### 2.1 Solar Radiation Measurement

Extraterrestrial solar radiation measured by satellite is  $1.36 \text{ kW/m}^2$  with an annual variation less than 0.1%. This incidence is attenuated when it reaches the ground level because of the interaction between the solar beam and the atmosphere. This interaction divides the extraterrestrial beam into two components (in Fig. 2.1): Direct Normal Irradiance (DNI) and Diffuse Irradiance (DIF). As a result, the Global Horizontal Irradiance (GHI) received at ground level consists of both DNI and DIF:  $\text{GHI} = \text{DNI} \cos(\theta) + \text{DIF}$ . In general, the power of photovoltaic generators is linearly related to GHI, while the power of concentrated solar power generators depends almost entirely on the DNI.

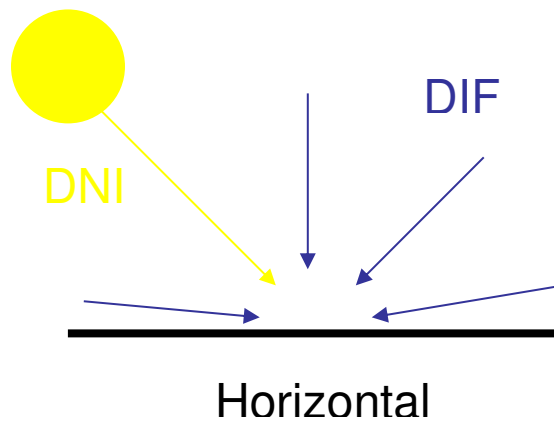


**Figure 2.1** The components of solar irradiance onto a horizontal surface at ground level: the attenuated direct irradiance and diffuse irradiance.

The demands for accurate solar radiation measurements from climatology, agriculture, and especially the rapidly growing industry of solar energy have motivated

the development of broadband solar radiation detectors. These detectors are usually based on three kinds of sensors: absolute cavity, thermopile, and photodiode.

The absolute cavity radiometer is a self-calibrating sensor based on the electrical substitution method first developed by Angstrom in 1893. The principle of absolute cavity is to compare the optical radiation heating to the electrical Joule heating. There are two key components of an absolute cavity sensor: (1) an absorber that has high absorption and is linked to a constant temperature sink and (2) a cavity that shields the absorber from other sources of radiation. The temperature of the absorber increases as radiation falls on it. Then the substituting electrical current heats the absorber to the same temperature without the radiation so that the electrical power equals the radiant power.

The cavity can be cooled to a cryogenic state to further increase the accuracy of the absolute cavity sensor. There are four ways in which the accuracy can be increased: First, compared to the room temperature, the specific heat of the cavity will decrease by a factor of 1,000, which will decrease the response time constant from a few hours to about three minutes at 4K. Second, the cryogenic state creates a superconducting connection that largely reduces the heat dissipated through the connecting wires and leads. Third, the radiative loss from the cavity follow the Stefan–Boltzmann law, so at room temperature the radiative loss may reach 10% of the input radiation, which will introduce a high measuring uncertainty. At 5K, the radiative loss is reduced to less than one-millionth of the input radiation, and the error introduced by the radiative loss is minimized. Fourth,

the cryogenic state fluid ideally guarantees the stability of the sink temperature.

Absolute Cavity Radiometers (ACS) that use absolute cavities as the sensors are used as the absolute standard of radiation measurements. The World Radiometric Reference (WRR), located at the Physical Meteorological Observatory in Switzerland, establishes the standard solar radiation measurement scale with an absolute cavity radiometer. The overall uncertainty after considering radiative loss, nonequivalence between solar and electrical heating, and other affections are expected to be less than 0.35%.

Radiation measurement instruments with absolute cavity sensors achieve high accuracy. Nevertheless, they require high setup and maintenance costs. Thus, most in-field solar detection instruments for both academic and industry applications use thermopile or photodiode as radiation sensors.

A thermopile is an electronic device made of several connected thermocouples, which are able to convert a heat gradient into a voltage signal based on thermoelectric effect (the Seebeck effect). The thermoelectric effect, first discovered by Seebeck in 1821, occurs when applying one end of a conductor to a heat source and maintaining the other end at a lower temperature; the temperature gradient along the conductor then generates a voltage between the two ends. The magnitude of the voltage depends on the Seebeck coefficients of the conductor's material. A device with a pair of different conductors is called a thermocouple. By measuring the voltage difference produced by the two



conductors, the temperature of the heat source can be estimated. Thermocouples are connected into a series to create a thermopile to acquire a higher output voltage signal.

Thermopiles are interchangeable and reliable. Thus, they are applied in many areas, especially in sensors such as radiation detection, heat flux sensors, gas or burner safety controls, magnetic sensors, vacuum sensors, flow sensors, etc. However, thermopile detectors still require significant capital costs. Photodiode-based detectors respond quickly, connect easily to electronics, and therefore are often used as a cheaper alternative to measure the irradiance with compromised accuracy.

A photodiode is a semiconductor diode that converts photon energy directly into electrical energy. A silicon solar cell can be regarded as a photodiode with a large area. The photodiode is usually designed as a PIN junction, which can work in two modes: photovoltaic and photoconductive. The photovoltaic mode does not require an applied bias. The flow of photoelectrons generates a forward bias similar to the one generated by a solar cell. However, the dependence of this voltage on light power is nonlinear. The photoconductive mode requires a reverse bias to the PIN junction. The reverse bias increases the width of the depletion layer, which decreases the junction's capacitance, resulting in reduction of response time. This mode has a linear response to the radiation intensity at the expense of increased noise. The photodiode only responds to photons with a wavelength shorter than the cutoff wavelength of the PIN junction, and it has different responsivity to photons of different wavelengths. Therefore, the nonlinear spectrum

responsivity of the photodiodes leads to an increased rate of error.

Pyranometers or pyrhemometers are common in-field devices which use either thermopiles or photodiodes as the irradiance sensors for solar measurements.

Pyranometers are designed to measure the irradiance on a plane surface with  $2\pi$  steradian of observation angle, which includes the direct and diffuse irradiance. Pyranometers are able to capture the information of GHI, DNI and DIF with a shadow band or ring. Many commercial pyranometers are thermopile-based (Fig. 2.2 (a)). They have nearly constant response across the broadband spectrum. Therefore, they achieve great accuracy and are widely used as the secondary standard instruments. Due to the consideration of cost and respond speed, photodiode sensors are widely employed in pyranometers (Fig. 2.2 (b)). Nonetheless, their measurement has higher uncertainty due to the photodiode sensor's nonlinear spectrum responsivity. As a result, photodiode-based pyranometers are used as an economical option for radiation measuring applications that require relatively loose accuracy.

Pyrhemometers are designed to measure the DNI. They detect a five-degree angle of view, so trackers are necessary to keep the pyrhemometers pointed to the Sun. A pyrhemometer consists of a collect window, which can filter the radiation and protect the detectors inside; a shield, which keeps the system from the influence of wind and ambient temperature; and a sensor that can be either a thermopile or photodiode. Sensors of pyrhemometers are usually based on thermopiles. Photodiodes are also being applied, and

they share the same advantages and drawbacks as their counterparts in pyranometers.

Eppley thermopile pyranometers and Eppley thermopile pyrhemometers (Fig. 2.2 (a) and (c)) are deployed at our research group's observatories in Merced, and San Diego, California.

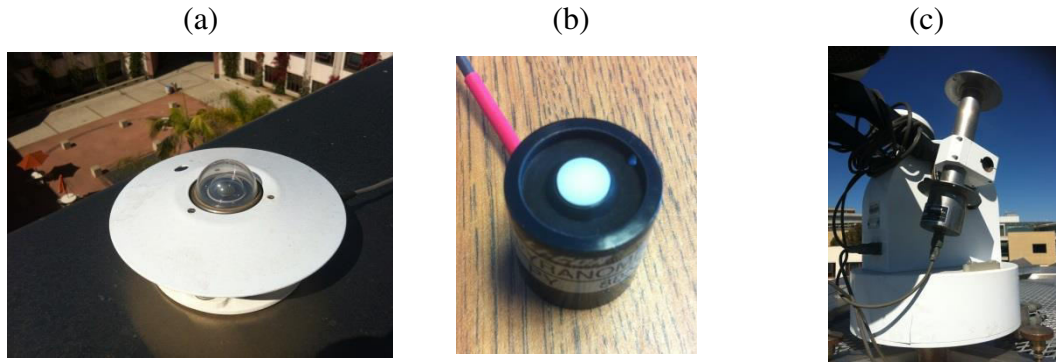


**Figure 2.2** Solar measurement instruments: (a) Eppley thermopile-based precision spectral pyranometer; (b) LI-COR photodiode based pyranometer; (c) Eppley thermopile-based normal incidence pyrhemometer mounted on a Sun tracker.

## 2.2 Sky Imaging Techniques

Clouds play an important role in the radiative balance of Earth's atmosphere. Observing the sky and extracting cloud cover information is critical to studies of radiation modeling and forecasting. Cloud information can be studied with satellite images (Rossow and Schiffer (1999), Zhao and Di Girolamo (2006), Marquez et al. (2013)). However, both spatial and temporal resolutions of satellite images are limited (Ghonima et al. (2012), Marquez and Coimbra (2013)). Ground-based sky imagers (SI) have been developed to capture high resolution sky images locally (Johnson et al. (1988), Voss and Zibordi (1989), Shield et al. (1993), Shield et al. (1998), Souza-Echer et al. (2003), Li et al. (2004), Long et al. (2006), Siez et al. (2007), Calbo and Sabburg (2008),

Mantelli Neto et al. (2010), Chow et al. (2011)).

Sky imager such as Yankee Environmental Systems (YES) Total Sky Imager (TSI-880) (shown in Fig 2.3) is a representative automatic, full-color, sky-imaging system that provides real-time processing and display of daytime sky conditions. It is composed of a rotating hemispherical mirror that reflects an image of the sky onto a CCD camera located above the mirror. A shadow band, which is located on the rotating mirror, blocks the direct component of the irradiance and protects the camera from damage, which can result from high intensity saturation of the CCD. The TSI 880 has built-in image processing software that performs tasks such as cloud classification and Sun percentage (SP) calculations. SP is the percentage of daily images in which the Sun is shining, and these values are used to classify the weather type for a given day of interest.

The Vivotek FE8171V Vandal-Proof Fish-eye Network Dome Camera is proposed as an alternative to capture the sky image (shown in Fig. 2.3). For the sake of brevity, from here on, this instrument is denoted as SkyCam. The SkyCam is equipped with a fish-eye lens that offers a  $180^\circ$  panoramic view. This camera includes a 3.1 MP-resolution sensor that delivers images at a resolution of 2048 x 1536. SkyCam are installed at multiple observatories located in California. Details about the application of the SkyCam will be presented in Chapter 4.



**Figure 2.3** The sky imaging devices. Yankee Environmental Systems (YES) Total Sky Imager is quoted by red square; Vivotek FE8171V Vandal-Proof Fish-eye Network Dome Cameras are quoted by yellow squares.

Images captured by sky imagers are mostly recorded as red-green-blue (RGB) color images. On these images, cloud pixels usually have higher red (R) intensity values than sky pixels. Therefore, cloud and sky pixels can be distinguished with a threshold through automatic cloud-identification methods with either fixed or adaptive thresholding techniques (Johson (1988), Koehler et al. (1991), Shields et al. (1993), Souza-Echer (2006), Long et al. (2006), Yang et al. (2009), Heinle et al. (2010), Mantelli Neto et al. (2010), Li et al. (2011), Ghonima et al. (2012)). The accuracy of these algorithms can exceed 90%, depending on cloud cover genre. Several representative cloud detection methods are discussed below.

Fixed thresholding method (FTM). FTM calculates the ratio ( $RBR = R/B$ ) or difference ( $RBD = R - B$ ) of red intensity to blue intensity for each pixel in an image and compares the ratio/difference with a fixed threshold to determine whether a pixel

corresponds to cloud or clear sky. An alternative to these two quantities is the normalized RBR ( $\text{NRBR} = (R - B)/(R + B)$ ). NRBR shows improved robustness to noise because it avoids extremely large RBRs when pixels have very low blue intensities (Li et al. (2011)).

FTM performs very well for clear or overcast images, but it is incapable of detecting thin clouds such as cirriform (Li et al. (2011)). Li et al. (2011) shows that the Minimum Cross Entropy method (MCE) achieved better performance than the FTM in identification of cumuliform and cirriform clouds. The MCE is an adaptive thresholding method based on the Otsu algorithm (Li and Lee (1993), Li and Tam (1998), Li et al. (2011)). Once the threshold is determined, pixels with higher RBR than the value of MCE-threshold are classified as cloudy.

When the Sun is presented in an image, the RBRs of circumsolar pixels increase and likely to be misclassified as cloud. This phenomenon is denoted as “image glare” in Chu et al. (2014). The increase of RBR is highly dependent upon solar geometry and can be mostly circumvented by utilizing the clear sky library (CSL) method (Ghonima et al. (2012)). CSL is a database of previously captured clear sky images for different solar zenith angles. It is used to remove the geometric variation of clear sky RBRs that depend on the Sun-pixel angle and the solar zenith angle. CSL offsets the RBR of each pixel from the input image by the reference clear-sky RBR that corresponds to the same zenith angle, generating a DIFF image:  $\text{DIFF} = \text{RBR} - \text{CSL}$ . Then, FTM or MCE methods can

then be applied to the DIFF image to detect the clouds.

A smart adaptive cloud identification system (SACI), which integrates the FTM, MCE, and CSL methods, are developed specific for the SkyCam by Chu et al. (2014). The details of this SACI are discussed in Chapter 4.

## **2.3 Stochastic Learning Methods**

### **2.3.1 Artificial Neural Network**

A physical model might be complex to describe a dynamic system, and the error from each modeling step may accumulate to a noticeable level. Therefore, based on the idea of system identification, stochastic learning methods are used to build mathematical relations directly between the system behavior and external influences. Artificial Neural Network (ANN) is one of the stochastic learning tools to build such mathematical relation.

Multilayer perceptron is reported as one of the most successfully applied ANNs in literature for numerous studies of short-term solar forecast (Inman et al. (2013)). The key elements of the neural network are the neurons, which are interconnected and placed in layers (as shown in Fig. 2.4). The layers between the first input layer and last output layer are called hidden layers. In the case of perceptron, only forward connections are allowed. A Neuron on each hidden layer adds a bias  $\theta$  to the weighted inputs  $w_i X_i$  received from the previous layer and computes the sum  $z$  (Eq. 2.1). For each neuron, an activation function, usually nonlinear, such as the Sigmoidal function (Eq. 2.2), processes the sum

and generates the neuron's output. Then the output is used as the input for neurons in the next layer.

$$z = \sum_{i=1}^N w_i X_i + \theta \quad (2.1)$$

$$f(z) = \frac{1}{1+e^{-z}} \quad (2.2)$$

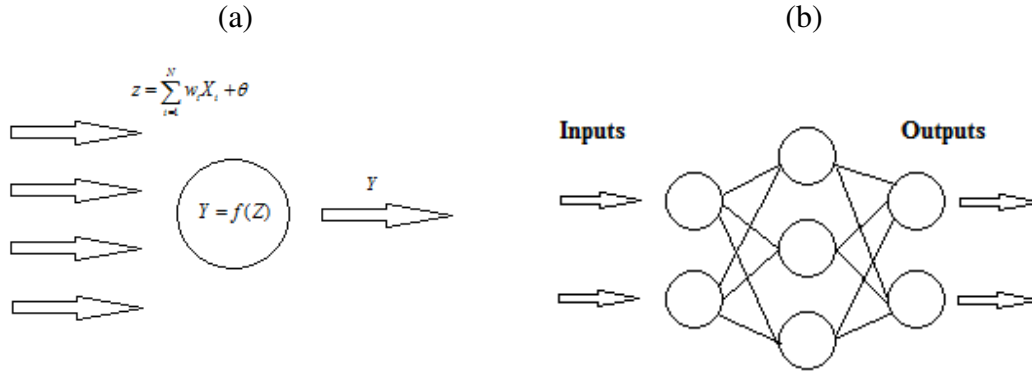


**Figure 2.4** (a) The basic function of a neuron. The neuron sums the weighted inputs  $x_i$  and uses an activation function to generate the output  $y$ . (b) An example of feed-forward neural network. Neurons are interconnected and placed in layers and the layers between the input layer ( $x_{pi}$ ) and the output layer ( $y_{pi}$ ) are called hidden layers.

ANN is a universal approximating function. Once the ANN architecture is determined, weight and bias values associated with each neuron must be estimated through a supervised training process using relevant data. These relevant data are called the learning/training data, which contain inputs and targets. The ANN takes the inputs and calculates the outputs with randomly assigned the initial weights and biases. An error (usually MSE) is generated by comparing the ANN's outputs to the targets. Then, the weights and biases are adjusted to minimize the error. This is an iterative process that stops once the error is lower than a preset threshold.



### 2.3.2 Validation Methods

During the ANN training, over-fitting might happen when the solution found in the training process fits the training data very well but performs poorly when applied to new data. Over-fitting can be addressed through a validation process. Two validation methods can be employed: the Cross Validation Method (CVM) and the Randomized Training and Validation Method (RTM).

CVM is widely used for determining whether a hypothesis model fits the data of interest. CVM divides the learning data into  $K$  disjoint subsets.  $K$  is usually set to 10 as suggested in previous studies (Kohavi (1995)). After partitioning the data, one subset is reserved for validation and the others are used for training of ANN. This process is repeated  $K$  times, while each time takes a different subset as the validation set and generates one error. The average of  $K$  times' errors is taken as the error of CVM validation. An example of 3-fold CVM is illustrated in Fig. 2.5.

### One iteration of a 3-fold cross-validation

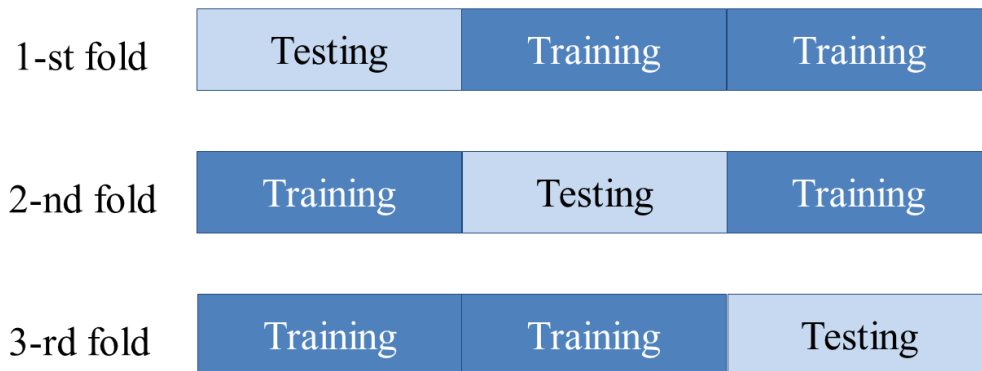


**Figure 2.5** An example of 3-fold cross-validation method. The learning data are divided into three subsets, one of which is reserved for validation and the others are used for training of ANN. This process is repeated for 3 times, each time taking a different subset as the validation set.

RTM is a new training process proposed by our research group. RTM is a learning process that selectively chooses part of the learning period for training. It is based on the premise that not all elements of the available data are equally informative for ANN training (e.g., outliers or repeated data points). Moreover, this strategy searches for the optimal composition of the training and validation sets by means of some optimization algorithm such as Genetic Algorithm (GA). GA will be discussed in the following section.

The RTM includes five steps:

1. The learning period is divided into separated training and validation sets (usually with a ratio of seven to three).
2. The training set is further divided into 100 divisions of equal size.
3. Several divisions of the training set are selected randomly to train the ANN.

4. The trained ANN is validated on data randomly selected (usually from 5–100%) from the predetermined validation set.
5. The validation process is conducted for K times, and the average of the K errors is computed as the error of RTM validation.

A good model should have a low validation error using either CVM or RTM. High error identifies a model whose performance is very dependent on the training data. Therefore, this model is prone to overfitting issues.

### **2.3.3 Genetic Algorithm**

There are many possible inputs which are potentially useful to forecast solar irradiance. Consequently, there are numerous ways to select the optimal combinations of inputs to the ANN; together with the number of possible ANN hierarchies, the quantity of the ANN variations for certain forecast purposes is substantial. Calculating validation errors of all possible ANN schemes to identify the best scheme is computationally prohibitive. Therefore, Genetic Algorithm (GA) is employed to find the optimal model.

GA is inspired by the idea of natural selection and survival of the fittest. First introduced by Holland (1975), it is widely used as an efficient optimization tool (Mellitt (2008), Marquez & Coimbra (2011)). The GA is an iterative process that scans elements of the search space to find the global optimum. The iterative process is based on the fitness of each individual who is represented by a vector of assigned optimization parameters. In general, GA starts with a random set of individuals who cover the search

space uniformly. An objective function based on CVM or RTM evaluates each individual and calculates a validation errors as its fitness. The ones with relatively lower validation errors are selected as parents for the following generation of individuals who are created through crossover and mutation. The iterative process continues until the fitness of the best individual converges with the average fitness of the entire population (shown in Fig. 2.6).

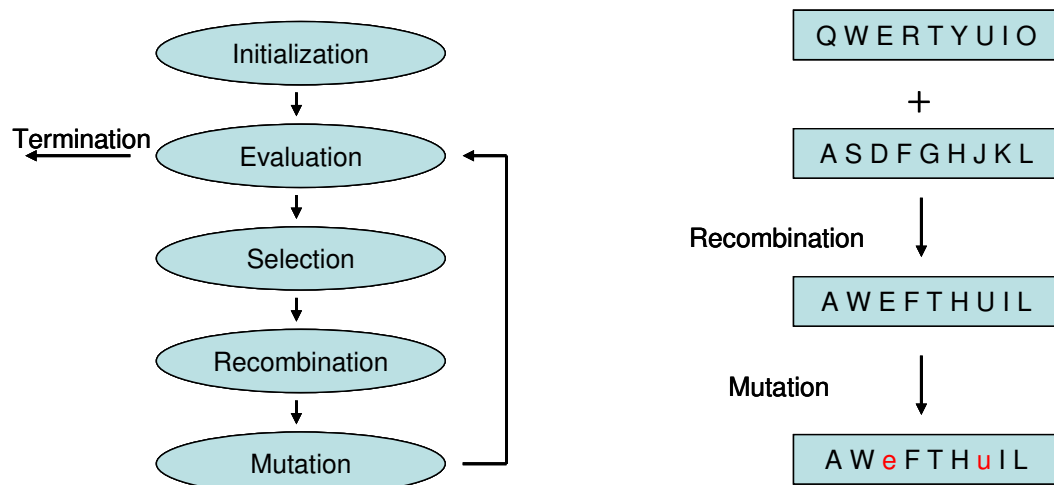


**Figure 2.6** a) The iterative activities of the population during generations. The performance of individuals of the population is evaluated by the optimization objective function, and the ones with lower error rates are selected to create the individuals of the next generation. b) The illustration of the recombine and mutations. The descendants' optimization parameters are a recombination from their parents, and the mutation will occur to segments of the descendant population based on preset parameters (Mellit (2008)).

When using the CVM method, the GA optimization considers the combination of subsets of inputs and ANN architecture (L and N) as the optimization parameters. When using RTM, the composition of the training set is added to the list of parameters to be optimized, which means that the search space for the RTM is much bigger. For that

reason, a population of 50 individuals is suggested for the first case and a population of 100 individuals is suggested for the second case.

### 2.3.4 Support Vector Machine

SVM is a useful tool for pattern recognition and data classification (Melgani and Bruzzone (2004), Chang and Lin (2011)). LIBSVM tool box provided by Chang and Lin (2011) is used. SVM first maps the input vector  $x$  to a feature space where the input vector is associated with a class label  $y$  (0 or 1).

The inputs of SVM should be linearly scaled. In this dissertation, number of input features to SVM is usually greater than 10. Therefore, the linear kernel function is used as suggested by Chang and Lin (2011). SVM uses a hyperplane to separate these two classes of vectors:

$$f(x) = w \cdot x + b, \quad (2.3)$$

where  $w$  is a vector perpendicular to the hyperplane and  $b$  is a bias term. The optimal hyperplane is determined using a cost function that minimize the misclassification cases and maximize the margin between the closet support vectors and the hyperplane:

$$F(w, \varepsilon) = \frac{1}{2} ||w||^2 + C \sum_{i=1}^N \varepsilon_i, \quad (2.4)$$

where  $C$  determines the penalty assigned to misclassification cases  $\varepsilon$ , and minimization of  $F(w, \varepsilon)$  is subject to two constraints:

$$\begin{cases} y_i(w \cdot x_{i+b}) \geq 1 - \varepsilon_i, & i = 1, 2, \dots, N \\ \varepsilon_i \geq 0, & i = 1, 2, \dots, N \end{cases} \quad (2.5)$$

## 2.4 Assessment of Forecasts

Persistence model is selected as the reference model to benchmark all forecasts presented in this dissertation. To remove the effect of deterministic diurnal solar variation, clear sky index persistence model is used. This persistence model assumes that the clear sky index of irradiance or power generation remains constant between  $t$  and  $t+\Delta t$  resulting in the forecasting:

$$F_p(t + \Delta t) = \frac{T_{\text{clr}}(t+\Delta t)}{T_{\text{clr}}(t)} \times T(t), \quad (2.6)$$

where  $F_p$  is the persistence prediction for forecast horizon  $\Delta t$ , clr denote clear sky prediction provided by clear sky models. The clear sky model used is described in Ineichen and Perez (2002), Ineichen (2008), Chu et al. (2013), Quesada-Ruiz et al. (2014).

Four statistical metrics to assess the point predictions of all the analyzed models:

Mean biased error (MBE)

$$\text{MBE} = \frac{1}{m} \sum_{t=1}^m (F(t) - T(t)), \quad (2.7)$$

where  $F$  is the forecasted value and time  $t$ ,  $T$  is the target value.

Mean absolute error (MAE)

$$\text{MAE} = \frac{1}{m} \sum_{t=1}^m (|F(t) - T(t)|). \quad (2.8)$$

Root mean square error (RMSE)

$$\text{RMSE} = \sqrt{\frac{1}{m} \sum_{t=1}^m (F(t) - T(t))^2}. \quad (2.9)$$

Forecast skill ( $s$ ), which represents the improvement of forecast accuracy against the reference persistence model:

$$s = 1 - \frac{\text{RMSE}}{\text{RMSE}_p}, \quad (2.10)$$

where  $\text{RMSE}_p$  is the forecast RMSE for the reference persistence model.

Besides the above statistic metrics which are used to assess the performance of point forecasts. We also use three performance indexes (Khosravi et al. (2013)) to quantitatively assess the PIs:

Prediction interval coverage probability (PICP), which measures whether the target values are covered by the PIs:

$$\text{PICP} = \frac{1}{m} \sum_{i=1}^m c_i, \quad (2.11)$$

where  $c_i=1$  when measured value is within the PIs, otherwise  $c_i=0$ .

Prediction interval normalized averaged width (PINAW), which measures the informativeness of PIs:

$$\text{PINAW} = \frac{1}{m} \sum_{i=1}^m \frac{W_i}{T_{clr}}, \quad (2.12)$$

where  $W_i$  is the width between the upper bound and the lower bound of PIs, and  $T_{clr}$  is the clear sky value.

Coverage width-based criterion (CWC), which assesses the quality of PIs combining PICP and PINAW:

$$\text{CWC} = \text{PINAW}(1 + \gamma(\text{PICP})e^{\eta(1-a-\text{PICP})}), \quad (2.13)$$

where  $\gamma$  depends on the value of PICP:

$$\gamma = \begin{cases} 0 & PICP \geq 1 - \alpha \\ 1 & PICP < 1 - \alpha \end{cases} \quad (2.14)$$

where  $1-\alpha$  is the nominal confidence level,  $\eta$  is a parameter governing the weight of PICP in calculating the magnitude of CWC. Coverage probability (PICP) is the most important characteristic for PIs. Therefore,  $\eta$  is set to 50 to highly penalize invalid PIs as suggested in Khosravi et al. (2013).



### 3 Smart Forecasting Engine

#### 3.1 Methods

The development of the smart forecasting engine includes two steps: ANN training and GA optimization. ANN (multilayer perceptron) is applied as the core of the smart forecasting engine that statistically derives the mathematical relation between the inputs variables and the output. To optimize the ANN forecasting scheme, GA optimization is employed to find the optimal ANN scheme (architecture, inputs, and training process) for the forecasting engine. The object function of GA is the CVM validation method discussed in Section 2.3.2.

The ANN model is implemented in MATLAB using the Neural Network Toolbox 6.0. The ANNs are trained with the Bayesian regularization process that uses the Levenberg-Marquardt optimization to minimize the discrepancy between the ANN output and the targets. The ANN training process for a given ANN architecture is defined symbolically as:

$$(\text{ANN}_u(L, N), I, T) \xrightarrow{\text{Training}} \text{ANN}_B \quad (3.1)$$

where  $\text{ANN}_u$  represents the untrained feed-forward neural network that has  $L$  hidden layers and  $N$  neurons per layer. The inputs  $I$  and targets  $T$  are the learning data. The trained  $\text{ANN}_B$  (the forecasting model) is able to forecast with new inputs that have the same dimension as the learning inputs.  $I$  is a subset of all the possible inputs, which is determined by GA optimization.

The GA optimizations are submitted as parallel jobs to 10 cores (2.39GHz processor, 24GB RAM). Each optimization job takes about 1 day to complete. The GA optimization considers the selection of inputs and the ANN architecture (L and N) as the optimization parameters. An individual, representing a possible scheme for ANN, is evaluated on the learning data using CVM. The CVM validation error (discussed in Chapter 2.3.2) is assigned as the fitness of the individual. Individuals with the best fitness (lowest CVM error) give the highest forecast accuracy on the learning data and are less likely to be affected by over-fitting. Therefore, individuals with the best fitness are selected as parents for a new generation. The majority (80%) of the new population is created by crossing-over the parents and the remainder (20%) of the population is created via mutation. All the new individuals undergo the fitness calculation and this process repeats until the GA converges.

After obtaining the best individual that gives the optimal definition of the forecasting scheme on the learning data, the forecasting scheme should be tested on an independent data set to evaluate its performance when encountering new input data. A major concern at this step is the inconsistency of the ANN forecasts due to the random initialization of the ANN training. For instance, ANN-based engines trained with the same parameters on the same training set return different forecast results. This is caused by the existence of multiple local minima in the ANN training search space. Therefore, results from one single training process cannot be treated as repeatable. To avoid this

issue, the ANN is trained for multiple times, and each time uses the default random initialization and returns a forecasting ANN. The average output of these forecasting ANNs is defined as the output of the smart forecasting engine.

### **3.2 Case Study: Power Generation Reforecast from a 48 MWe Photovoltaic Plant**

Smart reforecast is performed by the smart forecasting engine to enhance the intra-hour power-generation forecast for Sempra Generation's Copper Mountain PV Plant. The smart reforecasting models, which are based on the smart forecasting engine, operate as adaptive Model Output Statistics (MOS) enhancers for three representative baseline models: a physical deterministic model (Det) based on local-sensing techniques, the autoregressive and moving average model (ARMA), and the k-th nearest neighbor model (kNN). The smart reforecasting models as well as their baseline models are evaluated on an independent testing set, and their performances are assessed in terms of common error statistics (mean bias, mean absolute error and root mean square error) and forecasting skill over the reference persistence model. The testing results show that the forecasting skills of the smart reforecasts (range from 11% to 27%) are significantly higher than their object models for the specific horizons of five, ten, and fifteen minutes. In this case study, for the first time, reforecasts are employed to enhance the intra-hour forecasting skills for power generation forecast models and this work demonstrates that the error of operational power generation forecast approaches is learnable, thereby reducible through appropriately optimized stochastic reforecasts.

Real AC power data is obtained from a 48 MW segment of Sempra Generation's Copper Mountain solar power plant (115.00°W, 35.79°N). The cadmium telluride thin film panels for the 96 inverters cover approximately 1.3 km<sup>2</sup> and are tilted at 25° with a due south azimuth. These 96 inverters provide an aggregate power for this 48MW segment. Power data is quality controlled by inspecting the output manually from each individual inverter for all days. Five weather stations provide standard meteorological measurements including plane-of-array GI and GHI from Kipp & Zonen MP11 broadband pyranometers.

Occasionally, measurement of a single inverter may not be available. As a result, the analyses and forecasts are always based on the average output of all available inverters. The sampling frequency of the power is one time per thirty seconds. The power time series, which is collected from Nov 1<sup>st</sup> to Dec 5<sup>th</sup>, is illustrated in Fig. 3.1, which shows that the period of analysis includes different types of weather. These data are archived by an OSIsoft PI Historian Server and transmitted to a similar server at the University of California, San Diego (UCSD).

The power generation and power forecast data are separated for model estimation, optimization, and evaluation: the first 15000 data points are used to estimate the three object models. The optimization schemes of Det, ARMA, and kNN will be determined on this set. The remaining data set are randomly divided into a learning subset making up 70% of the data and a testing subset making up 30% of the data. The learning set

(approximately 8,000 data points) is used for stochastic learning and GA optimization of smart reforecasting models, and the testing set (approximately 3,500 data points) is used to evaluate the performance of the optimized smart reforecast models as well as their baseline models, independent of the learning process.

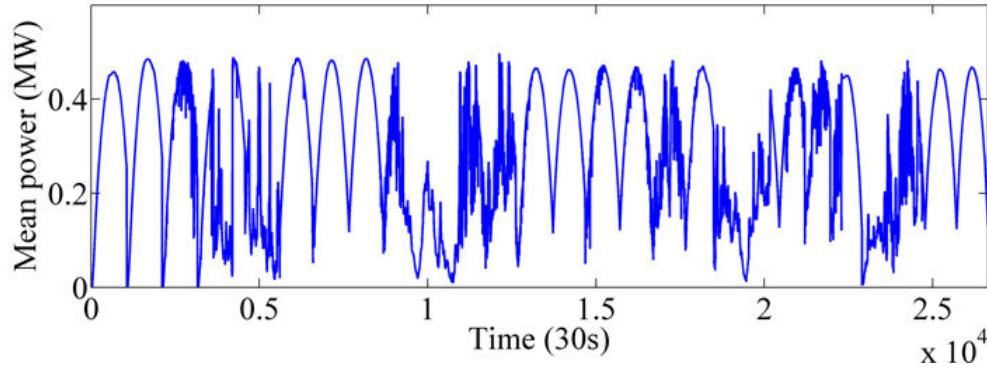


**Figure 3.1** The power series used in this case study. 28 days of forecasted data (11/01/11—12/05/11) utilize 26,638 time points. Night, early morning, and late afternoon periods, when power measurements are usually unavailable, have been excluded from analysis.

**Table 3.1** Testing results for 5-, 10-, and 15-minutes horizons. The highlighted numbers identify the best performing method for a given metric.

Horizon (min.)	MBE(kW)			MAE (kW)			RMSE (kW)			S (%)		
	5	10	15	5	10	15	5	10	15	5	10	15
Persistence	-1.1	-3.0	-3.0	21.9	30.6	33.7	41.8	52.7	57.6	0.0	0.0	0.0
Det.	-31.2	-26.0	-19.5	48.1	45.7	43.9	71.6	68.9	68.5	-71.3	-30.7	-18.9
Smart Det	<b>0.1</b>	-1.6	<b>0.1</b>	21.2	26.9	<b>27.1</b>	<b>35.5</b>	<b>41.2</b>	<b>42.5</b>	<b>15.1</b>	<b>21.8</b>	<b>26.2</b>
ARMA	-3.2	-6.7	-7.5	21.6	29.4	32.7	39.0	48.5	53.7	6.7	8.0	6.8
Smart ARMA	<b>0.1</b>	-1.5	1.2	<b>20.7</b>	<b>26.8</b>	29.3	36.4	44.1	46.4	12.9	16.3	19.4
kNN	-2.7	-7.4	-8.7	24.1	30.8	34.8	42.9	51.1	57.4	-2.6	3.0	0.3
Smart kNN	<b>0.1</b>	<b>-1.0</b>	2.5	21.2	30.8	29.9	37.1	45.3	46.4	11.2	14.0	19.4

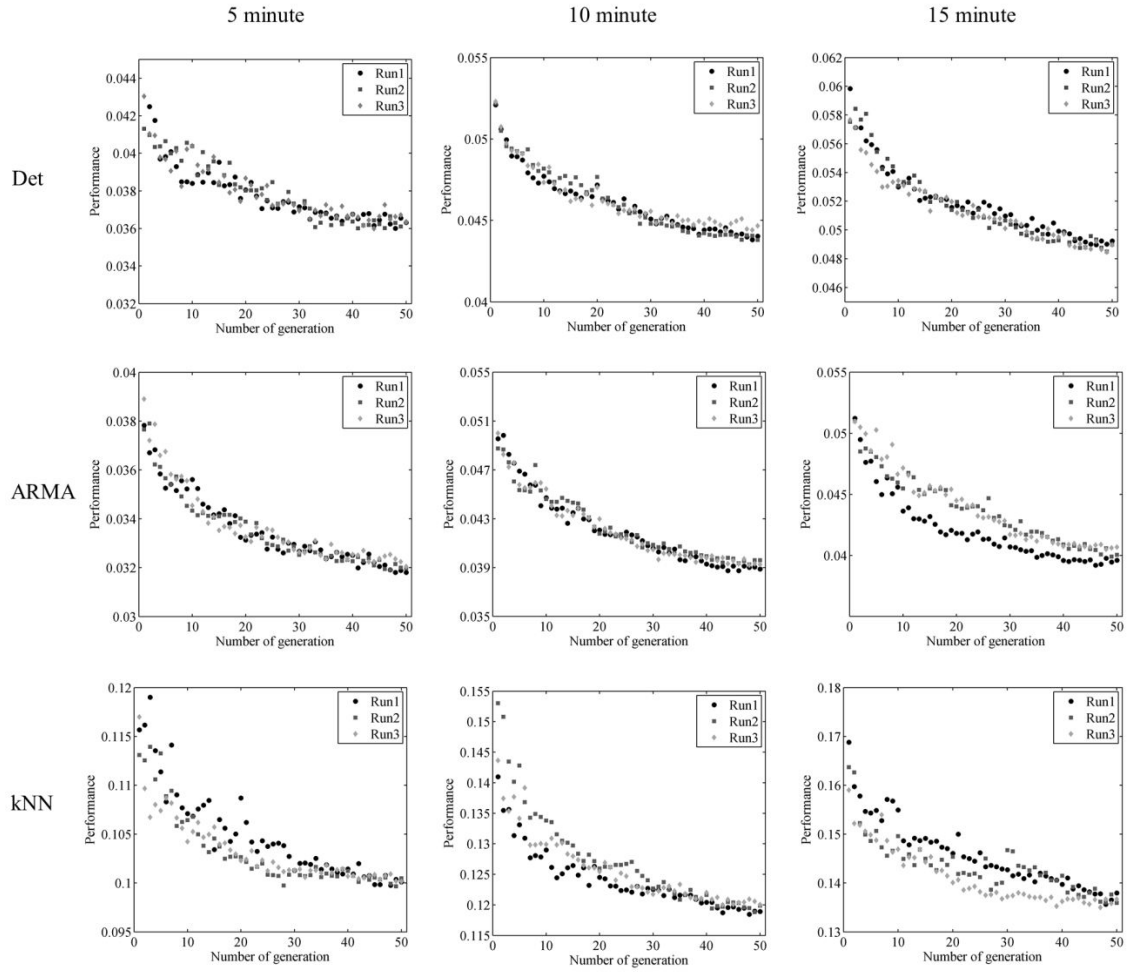


**Figure 3.2** Genetic algorithm identification of the optimal reforecast-ANN topology. All performance series are converged after 50 generations. GA under each situation has been performed for 3 times and the one with lowest performance is selected to determine the optimal topology of ANN.

Validation and GA optimization are used to search the optimal topology of the ANNs. GA is run for multiple times to ensure the consistency and robustness of its results (shown in Fig 3.2). Three reforecasting models, smart Det, smart ARMA, and smart kNN, as well as their object models, are evaluated on the testing set and compared to the persistence model. Their performance metrics are presented in Table 3.1. The results

show that each smart reforecasting model outperforms the persistence model and its object model, regardless of the forecast horizons. The testing RMSEs of all investigated models are illustrated in Fig. 3.3. The results indicate that the optimally trained smart model recognizes the forecasting error pattern of its object model, identifies the object forecasting bias, and achieves higher forecast skills.

The most prominent overall enhancement is made by the smart Det, which reduces the Det forecast RMSE by over 38% regardless of the forecast horizon (Fig. 3.3). This result shows that the smart Det benefits from integrating the cloud cover information and lagged power generation data. Smart Det outperforms the persistence model with forecast skills ranging from 15.1 to 26.1%, depending on the forecast horizons.

ARMA yields the highest overall forecast skills (around 7%) among the three baseline models. However, the RMSE reduction that smart ARMA demonstrated is the least among the three smart models (averagely 10%). The s of smart ARMA is significantly lower than the s of smart Det. The reason will be analyzed and discussed later.

The overall performance of the kNN forecast is parallel to the persistence forecast. The feature space of kNN only employs 15,000 data, which may not be enough to reflect all possible atmospheric conditions. The smart kNN achieves moderate RMSE reduction among the three smart reforecasting models. The forecast skill of smart kNN is inferior to both smart Det and smart ARMA. A larger collection of feature space is expected to

improve the performance of both kNN and smart kNN models.

To further understand the models' performances, their error ( $\epsilon$ ) distributions for the two investigated horizons are studied in Fig. 3.4 and 3.5, respectively. The standard deviation, Pearson's skewness, and kurtosis for each distribution are calculated and listed in Table 3.2. Standard deviation is used to quantify the level of the distribution's dispersion. Skewness is used to quantify the level of the distribution's bias, which is defined as the difference between the mean and mode divided by the standard deviation. For example, a distribution with a longer or fatter right tail than the left tail yields a positive skewness. Kurtosis is used to quantify the "peakedness" of a distribution and heaviness of its tail. The definition of Kurtosis is the distribution's fourth central moment divided by the fourth power of its standard deviation. For example, a distribution with a sharper peak and longer, heavier tails yields a high kurtosis.

**Table 3.2** Statistical results of the analysis for the error distributions.

<b>Horizon (min.)</b>	<b>Standard Deviation</b>			<b>Skewness</b>			<b>Kurtosis</b>		
	5	10	15	5	10	15	5	10	15
<b>Persistence</b>	0.0418	0.0527	0.0575	-0.0257	-0.0564	-0.0516	12.3055	8.3966	8.3158
<b>Det.</b>	0.0645	0.0638	0.0657	-0.4834	-0.4070	-0.2976	5.7441	5.6172	6.1051
<b>Smart Det</b>	0.0355	0.0412	0.0425	-0.0037	-0.0387	0.0032	10.6125	7.2039	6.6759
<b>ARMA</b>	0.0389	0.0481	0.0531	-0.0818	-0.1389	-0.1417	11.4599	8.6004	8.2282
<b>Smart ARMA</b>	0.0364	0.0441	0.0464	0.0019	-0.0348	0.0250	10.0702	8.1636	6.7361
<b>kNN</b>	0.0428	0.0506	0.0567	-0.0632	-0.1461	-0.1532	8.8997	7.3065	7.4041
<b>Smart kNN</b>	0.0371	0.0453	0.0464	0.0030	-0.0224	0.0536	9.0757	7.5650	6.2277



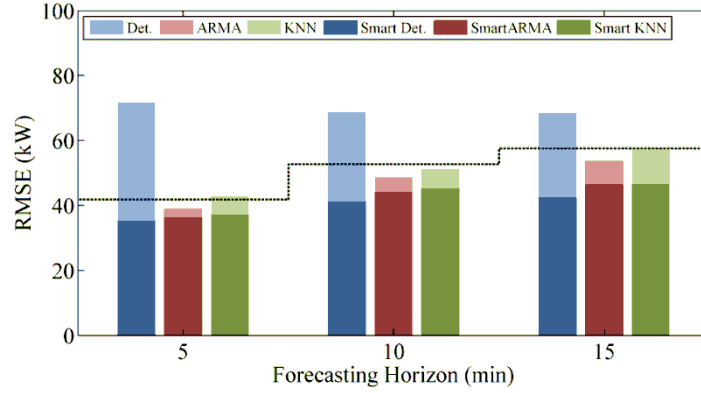


**Figure 3.3** Plot of testing RMSEs for 5, 10, and 15 minutes horizons. The bars with lighter color represent testing RMSEs for target models, and the bars with darker color represent smart forecast RMSEs. The dash line represents the persistence forecast RMSE for each horizon (Chu et al. 2015).

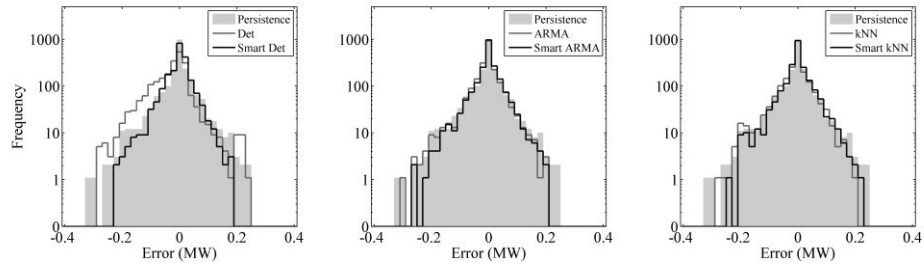


**Figure 3.4** Plots of error ( $\epsilon$ ) Distributions for 10 minutes horizon forecasts (Chu et al. 2015).

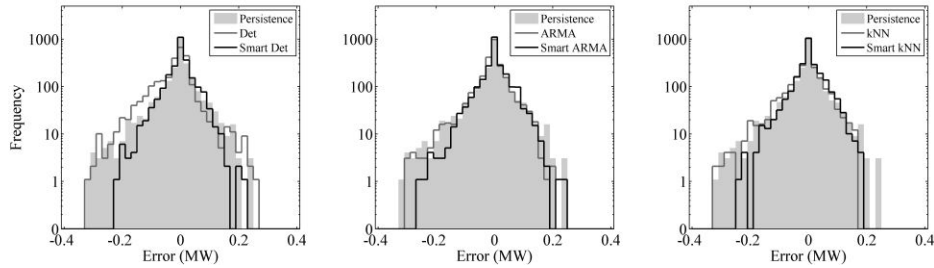


**Figure 3.5** Plots of error ( $\epsilon$ ) Distributions for 15 minutes ahead forecasts (Chu et al. 2015).

Persistence model: The negative skewnesses (from -0.026 to -0.0516) of persistence error distribution indicates that these distributions lean slightly to the left side for all the three forecast horizons. It has a moderate level of deviation but the highest

kurtosis, indicating that it has the sharpest peak. This is the result of excellent performance of the persistence forecast for low  $V$  periods, which comprises more than 50% of the testing period. Nevertheless, persistence forecast performance degrades as  $V$  increases. Therefore, the distribution of persistence errors has fat tails, resulting in relatively high standard deviation.

Det and Smart Det: The error distribution of Det forecast shows a negative skewness with highest absolute value among all distributions ( $< -0.3$ ), which agrees with the highest magnitude of testing MBE ( $< -20$  kW). This result suggests that the Det is more likely to underestimate the power generations, resulting in overestimation of ramp rates, which is shown in Fig. 3.6a. The lowest kurtosis and highest standard deviation of the error distribution indicates a high RMSE. The error distributions of smart Det achieves the substantially lower magnitude of skewness ( $< 0.01$ ) than the Det for all forecast horizons, indicating that the smart Det identifies and reduces the systematic forecast bias. Because the smart forecast estimates a more reasonable ramp rate, it reduces the occurrence of high absolute value errors (shown in Fig. 3.6a). These together produce an error distribution with shorter tails, rounder shoulder, and a moderate kurtosis. Consequently, the smart error distribution is narrowed and results in lowest standard deviation and lowest RMSE.

ARMA and smart ARMA: ARMA forecast has a higher value of negative skewness than the persistence model, indicating it usually overestimates the power

generation. Its error distribution has a relatively low standard deviation and relatively high kurtosis, which represents a narrowed distribution with less occurrence of high absolute value error. This is due to the nature of the AMRA model that only considers the lag time series in the past half an hour. Thus, it estimates the ramp only as a more sophisticated persistence model with a longer forecast horizon. An example is presented in Fig. 3.6b, where the ARMA forecast time series follow the low frequency ramp, and this overall reduces the occurrence of high absolute value errors. Nevertheless, it misses the high frequency ramp that increases the occurrence of moderate sized errors. Based on the ARMA, which means that there is only lagged power generation information involved, the smart ARMA demonstrates similar characteristics and makes the least improvement among the three smart models. Smart ARMA identifies and reduces the systematic bias and produces a low skewness. However, smart ARMA do not improve the accuracy of ramp rate estimation as significantly as the smart Det (Fig. 3.6 .a and b). These together yield a right shift of the error distributions, which reduces the occurrence of negative errors with the side effect of a slight increase in occurrence of positive errors (shown in Fig. 3.4 and 3.5).

kNN and smart kNN: Because of the limitation in the size of the feature space, the forecast skill of the kNN forecast is parallel to the persistence forecast. And error distribution of the kNN forecast has relatively high standard deviation and absolute magnitude of skewness. Negative values of skewness are observed for all baseline

models, which can be explained by the fact that solar power gradually decreases in the studied season. The period (early Nov.) used for object model estimation has higher average clear sky irradiance than the testing period (late Nov. and early Dec.). Therefore, the parameters of baseline models determined on the estimation set tend to overestimate the power generation in the testing set. This tendency shows that seasonal factors shall be considered for all kinds of power generation forecasting models. Smart kNN improves the performance of its target model in the same way as smart AMRA. It has the lowest kurtosis and highest level of standard deviation among all smart forecasting models. An example can be seen in Fig. 3.6.c.

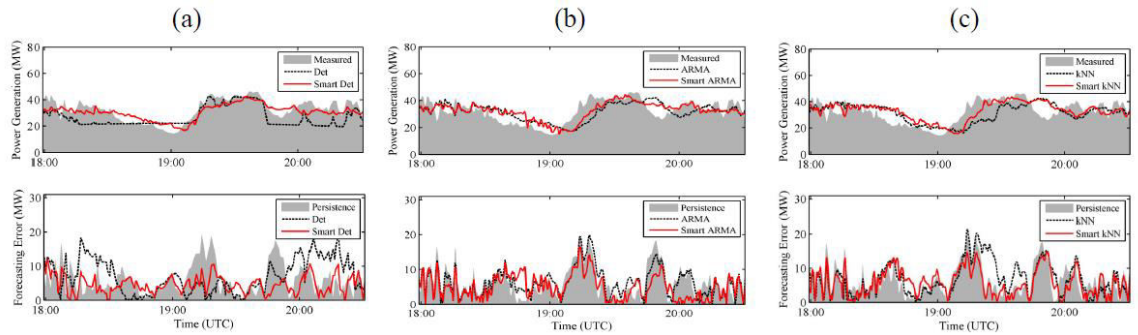


**Figure 3.6** Sample time series of forecasted power generation and absolute forecast errors: (a) deterministic and smart deterministic, (b) ARMA and smart ARMA, and (c) kNN and smart kNN. (Chu et al. 2015).

### 3.3 Summary

Smart forecasting engine is developed based on GA-optimized ANN and is employed in a case study to enhance the intra-hour generation forecasts for the operational Sempra Generation's Copper Mountain 48 MW PV plant. The evaluation on an independent testing set shows that the smart forecasting engine improves the baseline

forecasts in the following aspects:

1. Identifying the forecasting bias and substantially reducing the mean bias error.
2. Reducing the absolute forecasting error for moderate and high variability periods.
3. Decreasing the occurrence of large scale errors thereby narrowing the error distribution plot and improving the overall forecast skill for intra hour horizons

It is demonstrated that the smart forecasting engine, without adding any hardware costs, achieves a forecast skill that is significantly higher than the reference persistence model. These results reveal that: (1) the errors of operating forecasting tools (e.g. sky-imaging based model) is learnable and reducible through an appropriately optimized stochastic learning method and (2) the smart reforecast is highly beneficial to solar forecast as well as solar energy integration. This smart reforecast technique is useful to real-time forecasts for weather-dependent solar energy generation.

### **Acknowledgements**

Chapter 3, in part, is a reprint of the publication: Y. Chu, B. Urquhart, S.M.I. Gohari, H.T.C. Pedro, J. Kleissl and C.F.M. Coimbra (2015) “Short-Term Reforecasting of Power Output from a 48 MWe Solar PV Plant”, *Solar Energy* (112), pp. 68-77. The dissertation author was the first author of this paper.

## **4 Smart Adaptive Cloud Identification System**

### **4.1 Fish-eye Camera for Sky Imaging**

Most of the available local-sensing techniques are developed based on sky imagers (Johnson et al. (1988), Voss and Zibordi (1989), Li et al. (2004), Long et al. (2006), Mantelli Neto et al. (2010), Chow et al. (2011)) such as YESDAQ TSI-880. However, sky imagers are usually associated with high capital and maintenance costs. In addition, SIs incorporated tracking systems, which block the direct sunlight from penetrating the sensors. The tracking systems further increase the installation and maintenance costs. For instance, TSI-880 requires complex mechanical mechanism to track the shadowband, but the tracking system is error-prone and needs frequent adjustments and alignments. Furthermore, the TSI-880 requires proprietary software to access and transfer the captured images, which furthermore increase the costs to initialize the systems as well as modifications and adjustments of the source codes. Substantial reductions in costs are critical for more prevalent applications of ground-based sky observance.

Vivotek FE8171V, an off-the-shelf fish-eye network camera (the SkyCam, defined in Chapter 2.2), is proposed as an inexpensive alternative solution for sky imaging. The SkyCam equipped with a 3.1MP CMOS sensor offers a 360 degree panoramic view. Since early 2012, five SkyCams have been deployed at three observatories in California (Merced, San Diego, and Folsom) to provide sky images every minute during daylight

times. These images are accessed over a FTP connection, transferred to the UCSD server, and stored in a MySQL database. This process is fully automated and therefore does not require on-site staff. However, occasional cleaning of the fish-eye lens is necessary.

The cost of this camera is substantially lower than the research-orientated SIs. The additional advantages compared to SIs include resolution, usability, and the fact that these kinds of cameras do not use any moving parts. On the other hand, the optical effect of glaring on the dome, caused by the direct normal irradiance is an issue that needs to be addressed with these cameras.

None of the existing methods in literature, including those discussed in Chapter 2.2, is capable of solving the issue of glaring solely for SkyCam images. Therefore, a smart adaptive cloud identification system (SACI), which employs separate thresholding schemes, is developed to address the glaring issue for the fish-eye sky camera.

## **4.2 Methods**

To study an input image, SACI first utilizes a smart adaptive thresholding set (SAT) to classify the image into three categories: clear, overcast, and partly cloudy. Time series of global horizontal irradiance (GHI) are utilized to further enhance the performance and robustness of SAT. Once the category of the input sky image is determined, SACI employs the most appropriate thresholding scheme to classify each image pixel into either cloud or sky.

SAT integrates the clear-sky irradiance model thresholding method with the

hybrid thresholding method, which is capable of classifying each input image into three atmospheric categories. Clear-sky irradiance thresholding method (CSIT) first studies the lagged GHI time series at the time when the input image is captured. It identifies whether the image is clear or not. If the CSIT yields a positive return, the image is categorized as clear. Otherwise, the hybrid thresholding method will be employed to analyze the NRBR histogram and further classified the image as either unimodal or bimodal. Unimodal image is categorized as overcast, while bimodal image is categorized as partly cloudy.

Hybrid thresholding: Hybrid thresholding is proposed by (Li et al. (2011)), which categorizes images into two groups based on the NRBR distribution histogram of images: unimodal, which consists of single element (either clear or cloud), has a single and sharp peak in its NRBR histogram; bimodal, which consists of both cloud and sky elements, has more than one peaks and a large variance in its NRBR histogram. Unimodal and bimodal images can be differentiated by standard deviation of their NRBR. An image is classified as a bimodal image when its standard deviation of NRBRs is higher than a standard deviation threshold (SDT). Otherwise it is classified as a unimodal image. Nevertheless, clear image series gives a high deviation of the ratio histograms because the image glare on the camera's dome has high NRBR that parallel clouds. As a result, this standard deviation thresholding is unable to distinguish between the clear and the partly cloudy sky. Therefore, the clear sky irradiance model is introduced to separate clear images from partly cloudy images.



Clear sky irradiance thresholding (CSIT): Automatic clear sky detection based on solar radiation measurements is developed in recent years (Long and Ackerman (2000), Younes and Muneer (2007), Reno et al. (2012)). These clear sky detection methods usually consider five GHI criteria to make a decision: (1) Mean GHI ( $G$ ), (2) Max GHI ( $M$ ), (3) Length of the GHI time series ( $L$ ), (4) variance of GHI changes ( $\sigma$ ), and (5) maximum deviation from clear sky GHI slope ( $\Delta S$ ). In this case study, the CSIT analyzes the GHI time series of past ten minute time window and calculates the five criteria. Then the criteria are compared to their clear sky counterparts of the same period estimated by the Ineichen's clear sky radiation model (Ineichen (2008)). The investigated period is classified as clear when all the five criteria are satisfied. The thresholds of CSIT are similar to those proposed by (Reno et al. (2012)).

To maximize the accuracy of cloud identification, SACI applies separate cloud identification schemes to different image categories. Based on the discussion of FT, MCE, and CSL in Chapter 2.2, SACI employs FT for overcast images, CSL with a fixed threshold FT for clear images (CSL+FT), and CSL with a MCE for partly-cloudy images (CSL+MCE). The architecture of SACI is demonstrated in the Fig. 4.1.

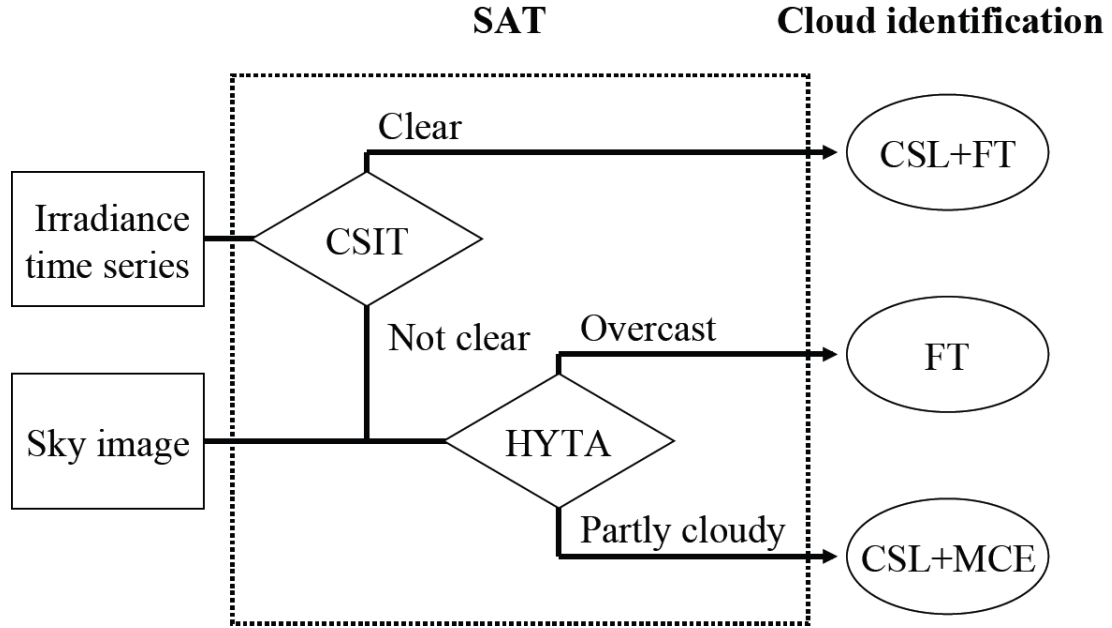


**Figure 4.1** Framework of smart adaptive cloud identification system (SACI). The dash square encloses the smart adaptive thresholding set (SAT). (Chu et al. 2014)

To evaluate the performance of SACI, each pixel from the cloud classification image is compared to its counterpart in the corresponded cloud map that is manually annotated. Using the confusion matrix shown in Table 4.1 for sky and cloud pixels, hits and misses is quantified in all the pixels in the image. Based on these values, the accuracy is defined as the percentage of pixels that are correctly classified:

$$\text{Accuracy} = \frac{\text{TP} + \text{TN}}{\text{TP} + \text{TN} + \text{FP} + \text{FN}} \times 100\% \quad (4.1)$$

**Table 4.1** Confusion matrix of automatic cloud detection for each pixel.

Algorithm classification	Manual classification	
	Cloud	Sky
Cloud	True positive (TP)	False positive (FP)
Sky	False negative (FN)	True negative (TN)

### 4.3 Case Study: SACI Cloud Detection for SkyCam Images

The proposed automatic smart adaptive cloud identification system (SACI) is employed to identify cloud cover for the images from SkyCams located in Merced and Folsom, California. The cloud detection scheme is optimized and validated against manually annotated images. The performance of the SACI is assessed in term of accuracy defined in Equation 4.1. Results show that SACI achieves overall classification accuracy higher than 90% and outperforms all reference cloud detection methods.

Sky images are obtained from two SkyCams deployed in two locations in California (Merced and Folsom). The SkyCams capture images every minute during daylight hours, and transfer them, via FTP, to a MySQL database on our server. Occasional cleaning of the SkyCam lens is necessary and images showing excessive dust on the dome are manually removed from the database.

80 images captured in Merced and 30 images captured in Folsom between March 5th and April 5th 2013 are used to develop and validate the cloud detection algorithm. These images represent diverse atmospheric conditions and each pixel in these images is manually classified into clear or cloud. The images from Merced are separated into a training set (50 images) and a validation set (30 images). All the images from Folsom are used as an independent validation set to study the generality of our models.

The training set is used to optimize the various parameters for the cloud detection algorithm: (1) the threshold of FT; (2) the threshold of CSL+FT; (3) the upper and lower

bound of MCE threshold; (4) the upper and lower bound of CSL+MCE threshold; and (5) SDT for the hybrid thresholding. Due to the distinct RBR distribution of each image category, none of the methods achieves high accuracy in all image classes. Identifying cirri/cumuliform clouds during partly-cloudy period is of primary interests in studies of intra-hour solar forecasts because these clouds are usually associated with high-frequency ramps in solar production. Therefore, the objective of training is to maximize the overall accuracies for partly-cloudy images. The optimal thresholds determined on the training set are shown in Table 4.2.

The training accuracies of methods with optimal thresholds are shown in the Table 4.3. The accuracies of both FT and MCE are over 95% for the overcast images and are over 85% for partly-cloudy images. CSL+FT achieves accuracies over 90% for clear images and partly-cloudy images. The new hybrid method CSL+MCE achieves the highest accuracy (92.7%) for partly-cloudy images among all models.

The mean of NRBR-SD for overcast images is 0.044 with a standard deviation of 0.007. As a result, the SDT is set to 0.075, below which is a 99.5% confidence interval that holds almost all possible overcast SD. This relatively high SDT may misclassify few broken sky periods as overcast periods.

Validation sets are used to evaluate all cloud identification models with determined thresholds. The performances are shown in the Tables 4.4 and 4.5 for the Merced validation set and Folsom validation set, respectively.

**Table 4.2** Optimal thresholds that maximize the cloud identification accuracy on the learning data set. The third column represents the threshold values used by the methods listed in the second column. SACI integrates the three reference methods and the SDT represents the standard deviation threshold for HYTA method. All thresholds are dimensionless.

	Thresholds	Values
<b>Reference methods</b>	FT	-0.11
	Bounds of MCE	0.15—0.40
	FT of CSL+FT	0.10
<b>SACI</b>	FT	-0.11
	FT of CSL+FT	0.10
	Bounds of CSL+MCE	0.08—0.2
	SDT	0.10

**Table 4.3** The results of training accuracy for cloud detection

		Clear	Overcast	Partly Cloudy
		Mean (Std)	Mean (Std)	Mean (Std)
FT	Accuracy (%)	63.8 (6.2)	<b>98.2 (1.8)</b>	86.0 (6.6)
MCE	Accuracy (%)	72.5 (6.1)	97.1(1.2)	86.3 (5.4)
CSL+FT	Accuracy (%)	<b>93.1 (1.8)</b>	51.5 (8.0)	91.0 (4.7)
CSL+MCE	Accuracy (%)	86.2 (6.2)	52.1 (7.2)	<b>92.7 (5.2)</b>

**Table 4.4** The validation results for validation images from Merced, California.

		Clear	Overcast	Partly Cloudy
		Mean (Std)	Mean (Std)	Mean (Std)
FT	Accuracy (%)	59.86 (7.6)	<b>95.8 (1.5)</b>	80.7 (10.6)
MCE	Accuracy (%)	53.0 (6.1)	93.7(2.0)	81.8 (10.4)
CSL+FT	Accuracy (%)	<b>92.2 (2.6)</b>	42.5 (3.0)	87.3 (3.7)
CSL+MCE	Accuracy (%)	87.4 (5.7)	50.0 (8.2)	<b>90.6 (3.2)</b>
SACI	Accuracy (%)	<b>92.2 (2.6)</b>	<b>95.8 (1.5)</b>	<b>90.6 (3.2)</b>

**Table 4.5** The validation results for validation images from Folsom, California.

		Clear	Overcast	Partly Cloudy
		Mean (Std)	Mean (Std)	Mean (Std)
FT	Accuracy (%)	55.3 (5.7)	<b>93.7 (3.0)</b>	89.2 (3.0)
MCE	Accuracy (%)	65.0 (3.5)	92.2 (3.2)	88.2 (3.9)
CSL+FT	Accuracy (%)	<b>94.5 (1.8)</b>	49.6 (8.8)	90.8 (7.2)
CSL+MCE	Accuracy (%)	89.5 (1.9)	54.9 (8.8)	<b>93.6 (1.6)</b>
SACI	Accuracy (%)	<b>94.5 (1.8)</b>	<b>93.7 (3.0)</b>	93.6 (1.6)

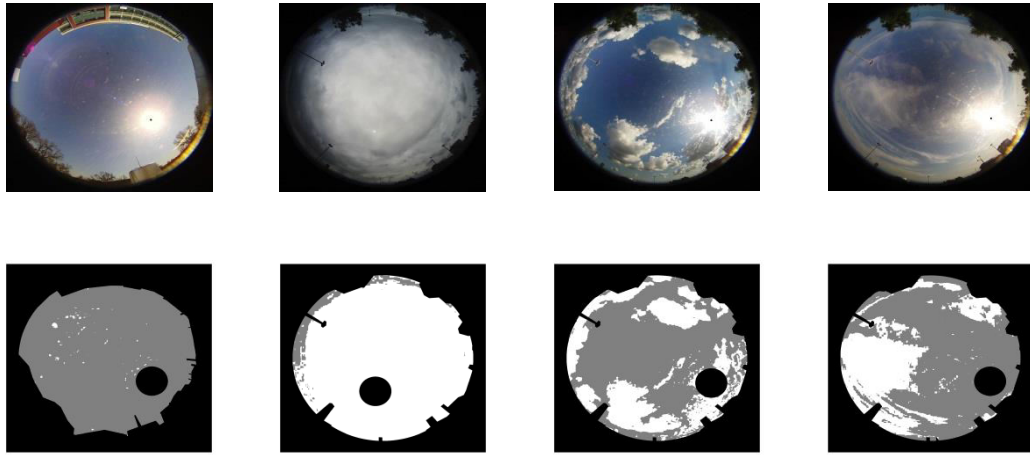


**Figure 4.2** Representative SACI cloud detection for clear, overcast, partly cloudy with optically thick, and optically thin cloud genres sky images. The top row is the original image and the bottom row is the classified binary cloud maps. White pixels represent cloud, gray pixels represent sky, and black pixels represent the masked region. (Chu et al. 2014)

The validation results show that only the SACI is able to achieve the highest overall accuracy for all different weather conditions (exemplified in Fig. 4.2). FT and MCE are unable to distinguish the dome glare from clouds during the clear period while CSL-based methods over-offset the RBR ratio image during the overcast periods. The SACI optimized with Merced images is directly applied to images captured at Folsom, and achieves parallel accuracy. This validates the universality and consistence of SACI

for all SkyCams of the same model when employed at different locations.

Compared with the visual inspection, the average accuracy of SACI for clear images is over 92%. Misclassification is usually caused by three reasons: (1) the RBRs of circumsolar region pixels saturate due to the glaring are not completely offset by CSL; (2) the improper diffraction of sunlight on the glass dome; and (3) the tiny taints, which diffract the sunlight intensively during the clear time.

The average accuracy of SACI for overcast images is 94%. Most misclassified pixels are located near the edge of the images (close to the horizon) where R intensities are not as high as their counterparts in the center of the images during overcast periods. Partly cloudy images usually contain both, thick and thin clouds. Thick cloud pixels generally have a RBR significantly higher than clear pixels, and therefore are detected easier by automatic algorithms. When the majority of clouds in an image are optically thick, the algorithm is on average over 95% accurate. On the other hand, thin clouds, whose RBRs are close to or overlap clear RBRs, are generally more difficult to be identified correctly. This comes together with the error associated with the manual cloud identification. This affects especially the edge regions of thin clouds. Thin cloud pixels generally have low identification accuracy, and the SACI algorithm is on average 85% accurate. Most of the misclassified pixels are false negative cases, which match our assumption that the algorithm is more likely to classify thin cloud pixels as sky pixel, particularly in the circumsolar region, where they are tend to be over-offset by high

magnitude CSL RBR resulting in a relatively low RBR that resemble clear sky pixels.

#### **4.4 Summary**

The smart adaptive cloud identification system (SACI) based on a generic fish-eye camera has been developed and deployed for multiple locations. This system integrates the fixed thresholding method, minimum cross entropy thresholding method and clear-sky library method. It addresses the issue of camera dome glaring solely by algorithm. The SACI first uses a smart adaptive thresholding set that considers the time series of global horizontal irradiance and a NRBR map of the input image to classify the captured sky images into three categories: clear, overcast, and partly cloudy. Then SACI employs the most suitable cloud detection scheme for each categorized image. Thresholds optimization is performed using manually annotated images. The validation tests for different locations show that SACI achieves robust, universal, and the most accurate cloud classification among all the reference models. Mean accuracies of this system are over 92%, 94%, and 89% for clear, overcast, and partly cloudy images, respectively.

It is demonstrated that this smart cloud detection system, with parallel performance to state-of-the-art cloud detection methods, is highly beneficial to all kinds of cloud observation applications such as climate or meteorology researches, weather and agriculture forecast, power generation forecast of solar utilities, etc.



## **Acknowledgements**

Chapter 4, in part, is a reprint of the publication: Y. Chu, L. Nonnenmacher, R.H. Inman, Z. Liao, H.T.C. Pedro, and C.F.M. Coimbra (2014) “A Smart Image-Based Cloud Detection System for Intra-Hour Solar Irradiance Forecasts”, *Journal of Atmospheric and Oceanic Technology* (31) pp. 1995-2007. The dissertation author was the first author of this paper.

## 5 Integrated Smart Forecasting Model

### 5.1 Methods

An integrated smart solar forecasting model (ISFM) is developed to predict one-minute averaged solar irradiance for intra-hour horizons. The ISFM integrates the ANN-based smart forecasting engine with either the TSI or SkyCam cloud detection system. Potential inputs to the ISFM includes: the time-lagged measured irradiance values, ranging from 0 to 30 min in steps of 5 min, the total sky cloudiness, and the numerical cloud indices  $CI_i$ , which is extracted from sky images (captured by either TSI or SkyCam) using a grid-cloud-fraction method.

The grid-cloud-fraction method is proposed by our research group (Marquez and Coimbra, 2012), and can be summarized in five major steps:

1. Images are projected from a convex mirror space into a flat rectangular space to mitigate the distortion caused by the mirror (shown in Fig. 5.1a and b).
2. Pairs of consecutive images are processed using Particle Image Velocimetry (PIV) to compute the mean flow direction of the clouds (shown in Fig. 5.1b).
3. A set of grid units ( $X_1, X_2 \dots X_6$ ) is placed over the images orienting in the reverse flow direction of the clouds from the position of the Sun (shown in Fig. 5.1c).
4. Cloud detection methods (Li et al. (2011), Chu et al. (2014)) are applied to identify the cloud cover on the images.
5. The cloud indices  $CI_i$ , which is the percentage of pixels classified as being clouds ( $CI_1$ ,

$CI_2 \dots CI_6$ ) in each grid element ( $X_1, X_2 \dots X_6$ ) are computed and are processed as inputs to the smart forecasting engine.

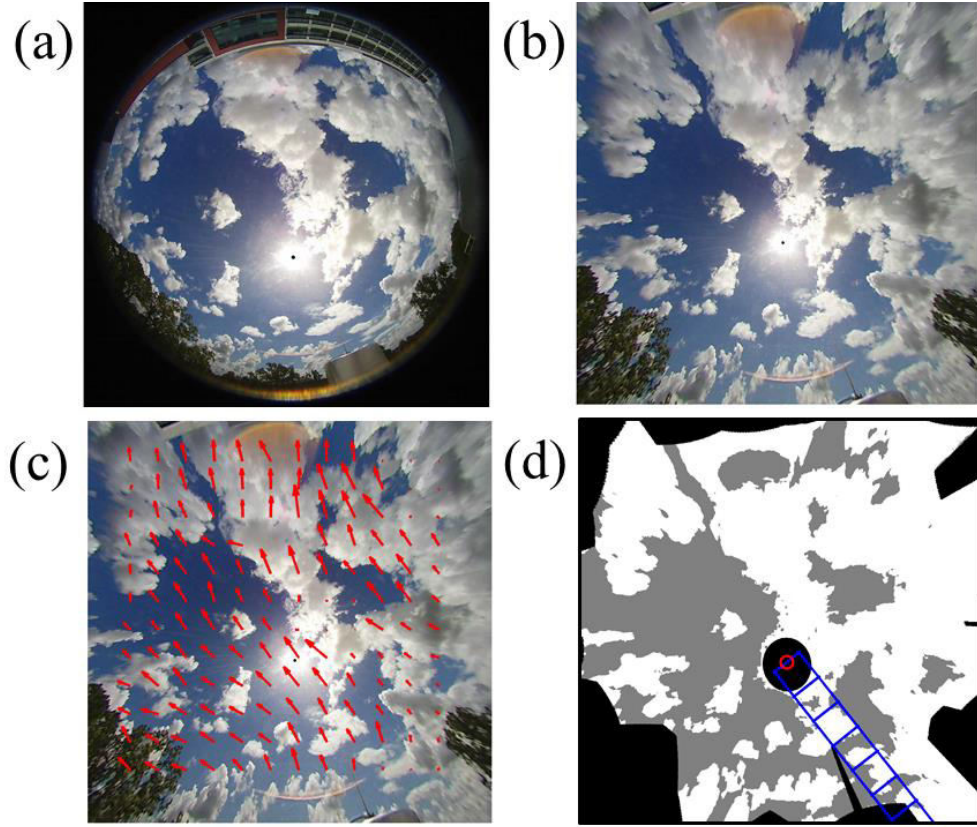


**Figure 5.1** Main steps of the cloud tracking method (Marquez & Coimbra, 2012): (a) the original sky image, (b) The image are projected onto a rectangular grid, (c) the velocity vectors computed by the PIV algorithm, and (d) the cloud classified image, where white pixels represent cloud, gray pixels represent clear sky, and black pixels are obstacle which are excluded from the analysis. The cloud indices  $CI_i$ , that is, the percentage of pixels classified as being clouds ( $CI_1, CI_2 \dots CI_6$ ) in each unit square ( $X_1, X_2 \dots X_6$ ) are computed for all grid elements and processed as inputs to GA-optimized ANN for short-term solar forecasts. (Chu et al. 2014).

Marquez and Coimbra (2013) propose a linear relation between each  $CI_i$  time-series and the forecast values of DNI, which is shown in Eq. 5.1:

$$B_i(t + \Delta t) = 0.9 \times (1 - CI_i) \quad (5.1)$$

where the factor  $0.9 \text{ kW/m}^2$  is an empirical constant for the peak DNI irradiance during the period studied in that paper. The obvious caveat for this model is that it only works well for times around the solar noon. To overcome this issue, a more generalized relation is used:

$$B_i(t + \Delta t) = B_{\text{clr}}(t + \Delta t) \times (1 - CI_i) \times P_o \quad (5.2)$$

The  $B_{\text{clr}}$  represents the clear sky DNI predicted by a clear sky model and the  $P_o$  represents the transmittance of the clouds.  $P_o$  is set to 1 because the algorithm only outputs binary cloud cover image. The performance of this deterministic model has been tested on four selected high DNI variance days, and it shows significant improvement over the persistent forecasting model.

The parameters of the ANN-based smart forecasting engine need to be estimated on learning data through supervised-training. The cross validation method (CVM) is employed to prevent over-fitting of the ANNs (Kohavi (1995), Chu et al. (2013)). The training data is divided into  $N$  subsets.  $N$  is set to 10 as suggested in literature (Kohavi (1995), Chu et al. (2014)). After the data partition, one subset is reserved for validation and the remaining subsets are used to train the ANN. Root mean square error (RMSE) is calculated as the performance of the model on the validation set. This process is repeated  $K$  times, each time taking a different subset as the validation set and returning a RMSE. The mean and variance of the  $K$  RMSEs are obtained as the CVM validation performance. Models with high mean and variance of the validation RMSEs are very dependent on the

training data and therefore prone to be overfitted.

The performance of the forecasting model depends on its input variables and the ANN topology (e.g. number of layers, number of neurons per layer). In order to obtain the best possible forecast, GA is used to determine these free parameters. GA is an efficient tool (Holland (1992), Marquez and Coimbra (2011), Pedro and Coimbra (2012)) that iteratively scans potential solutions (individuals) of the search space to find the optimal solution. GA optimization is initiated with randomly selected individuals (the population) whose fitness is evaluated according to an objective function. The GA optimization objective function is the CVM performance. The individuals with the lowest CVM validation error are selected as parents and generate the new generation through cross-over and mutation. This iterative process is finished when the average fitness of the population converges (indicated by the convergence of average GA fitness in about 50 generations). The GA is deployed with CVM validation method as the optimization objective function. The GA optimization considers the subsets of all inputs and ANN architecture (L and N) as the optimization parameters. A population of 50 individuals is used in the GA optimization.

In total, 12 elements are selected as GA inputs. The first 10 elements are binary, deciding whether a possible input should be selected as inputs to ANNs. The first five possible inputs are measured irradiance values on current time, 5 minutes ago, 10 minutes ago, 15 minutes ago and 20 minutes ago. The 6<sup>th</sup> possible input is the total sky cloudiness.

The last four possible inputs are cloud indices  $CI_1 \dots CI_4$ , calculated by the grid-cloud-fraction method. The goal of GA is to identify which possible inputs are more useful to the forecasts. The 11<sup>th</sup> GA input element is the number of hidden layers of ANN, which returns an integer, and the 12<sup>th</sup> GA input element is the number of neurons per hidden layer, which also returns an integer.

We submit GA optimizations work as parallel jobs to 10 cores (2.39GHz processor, 24GB RAM). The optimization and training work takes about 24 hours to complete. Once the optimized scheme is obtained via GA, the trained ANN takes new inputs and performs the forecasts in less than 1 second in real time.

## **5.2 Case study: ISFM Using TSI**

In this case study, the ISFM integrates the smart forecasting engine with the TSI cloud detection system to predict one minute average DNI for specific time horizons of five and ten minutes. The ISFM is developed and validated using six months of intra-minute imaging and irradiance measurements. The smart forecasting engine consists of two ANNs, which are developed for low and high DNI variability seasons, respectively. The methods used to develop season-specific ANN models consist of sky image processing, deterministic and ANN forecasting models, and GA optimizations. The ANNs trained for both seasons are used to build a seasonal-independent forecasting engine. An independent testing set is used to assess the performance of the ISFM. Performance is assessed in terms of common error statistics (mean bias and root mean square error), but

also in terms of forecasting skill over persistence.

Experimental data for this study are collected at our observatory in Merced (latitude = 37.36, longitude = -120.43), CA during the spring, summer and fall of 2011 (04/28/11 to 10/15/11). The DNI data are measured with Eppley Normal Incidence Pyrheliometer (NIP) every 30 seconds. Sky images are recorded with the Yankee Environmental Systems (YES) Total sky imager (TSI 880) every 20 seconds. The TSI is composed of a rotating hemispherical mirror which reflects the sky image onto a CCD camera. The images are saved in an online database from where they are retrieved and processed. The processing techniques used to transform the sky image into numerical cloud cover indices are explained in the next section. TSI built-in software computes the daily Sun percentage (SP) index, which gives an estimate for the fraction of daily images in which the Sun is shining. The daily SP values for the period analyzed are plotted in Fig. 5.2. These values were used to classify the type of DNI variability for a given day of interest.

One major concern in the TSI image processing system is the cloud detection during periods of high air mass time (when the Sun elevation is low during the first and last hours of the day). At these periods, higher scattering and diffusion of the solar beam is recorded in the TSI image as a large set of bright pixels in the circumsolar region. These pixels are often classified as clouds even in the case of completely clear sky. Therefore, to avoid incorrect classification of the image-processing algorithm, images

and data of early morning and late afternoon are excluded from the analysis. In other words, data points whose solar zenith angle  $\theta$  satisfied  $\cos(\theta) < 0.6$  will be excluded.

Merced has a Mediterranean climate with rainy winters and dry summers, as illustrated by the SP values in Fig. 5.2. In summer, the daily SP is close to 100%; spring is cloudy and the daily SP is relatively low; fall comprises significant numbers of both high and low SP days. The DNI data and sky images can be categorized into two very distinct phases: the low DNI variance phase, characterized by low variability of the DNI time-series and clear-sky conditions, and the high DNI variance phase characterized by high variability of DNI time-series and cloudy conditions.

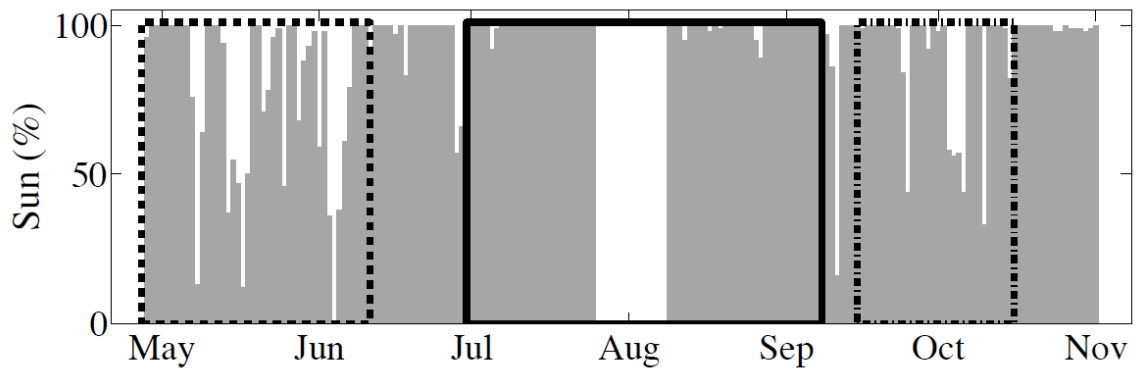


**Figure 5.2** The daily Sun percentage plot for the period from April 28, 2011 to October 30, 2011. Three subsets are created based on this plot: low DNI variance season (identified by the solid-line rectangle); high DNI variance season (identified by the dash-line rectangle); and independent testing set (identified by the dash dot line). (Chu et al. 2013)

Motivated by the very different levels of DNI variability among these phases, ANNs are trained specifically for each phase: low DNI variance ANN trained on summer's data and high DNI variance ANN trained on spring's data. In order to create



the models, spring and summer data were separated into two disjointed subsets: the learning set (70%) and the seasonal testing set (30%). The learning set is used to estimate the models, and the seasonal testing set is used to assess the performance of forecasting models for each season. We use fall's data, which contains both high and low variance periods of DNI, as an independent testing set to evaluate the proposed ISFM as well as two reference models: a persistence model and a sky-imaging based deterministic model (discussed in Eq. 5.2 (Marquez and Coimbra (2013))).

These two seasonal ANNs (for high and low DNI variability periods, respectively) are combined to create a season-independent smart forecasting model. This smart forecasting model is a piecewise function in which the cloud indexes CIs determine which seasonal forecasting model to use. When the sum of all CIs is zero (no clouds moving toward the Sun), it applies the ANN trained from low DNI variance season. Otherwise, it applies the ANN trained from high DNI variance season.

The test results of the persistence model, deterministic model (described in Chapter 5.1), and smart forecasting are shown in Table 5.1. These results show that the ISFM outperforms all other models regardless of the forecast horizon. Because the error level varies greatly from day to day depending on weather conditions, daily RMSE of the ISFM against the daily RMSE of the persistence models is plotted in Fig. 5.3. The resulting scatter plot is depicted for both 5- and 10-minute forecast horizons.

**Table 5.1** Forecast Performance for the Different Models Applied to the Independent Testing Set as a Function of the Forecasting Horizon (*boldface font identifies the best performance values*).

		5 minutes testing			10 minutes testing		
Models		MBE	RMSE	s	MBE	RMSE	s
		(W/m <sup>2</sup> )	(W/m <sup>2</sup> )		(W/m <sup>2</sup> )	(W/m <sup>2</sup> )	
09/15/11	<b>Smart</b>	<b>-0.15</b>	<b>88.6</b>	<b>0.209</b>	-1.9	<b>103.3</b>	<b>0.225</b>
to	Deterministic	-10.7	150.5	-0.256	-8.3	144.0	-0.074
10/15/11	Persistence	2.1	112.0	0	3.6	133.4	0

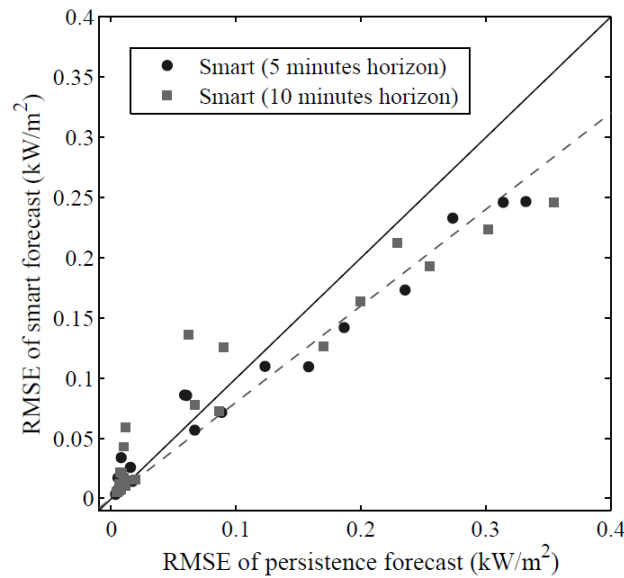


**Figure 5.3** Plot of daily RMSE of smart forecast against persistent forecast; each marker stands for one testing day. The solid line with slope 1 suggests an equal performance of hybrid forecast to the persistence forecast, and the dash line with slope 0.8 suggests that a border below that the forecasting skill of the hybrid model exceeds 20%. (Chu et al. 2013).

During similar  $V$  periods, the statistical quantities of forecast evaluation are comparable, and the ratio of absolute forecast errors to  $V$  is a statistical invariant for different forecasting models (Marquez & Coimbra, 2011). These ratios for persistence, deterministic and smart forecasts are plotted in Fig. 5.4. a and b for five and ten minutes

ahead forecasts respectively. The figures show that the persistence model is most accurate during low  $V$  periods ( $V < 0.1$ ) with absolute persistence forecast error close to zero. During these periods, the DNI time-series is very stable and ideal for persistence forecasts. However, the performance of the persistence model degrades considerably when  $V$  increases. The deterministic model shows superior performance for very high  $V$  periods for both five and ten minute forecasts. Nevertheless, its performance is inconsistent resulting in high absolute forecast errors for low  $V$  periods. The smart forecast is most accurate during intermediate variability conditions ( $0.10 < V < 0.25$ ). Moreover, its performance is nearly equivalent to the persistence forecast during low  $V$  periods, but slightly inferior to the deterministic forecast during high  $V$  periods.

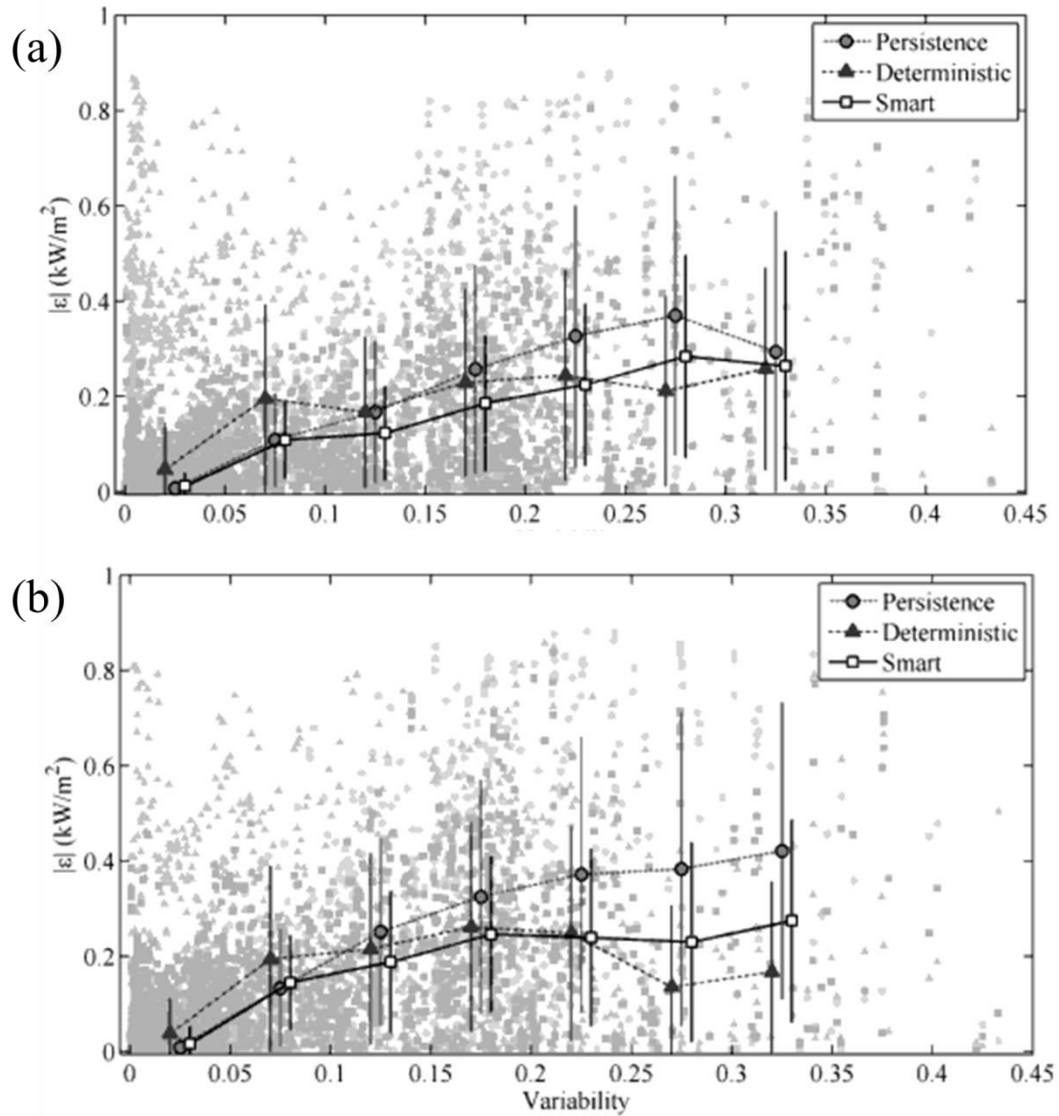


**Figure 5.4** Plot of absolute forecast error against DNI variability for (a) 5 minutes and (b) 10 minutes ahead forecasts. Round markers stand for persistence forecast, triangular markers stand for deterministic forecast, and square markers stand for smart forecast. The heavier markers are the mean absolute forecasting errors taken within the variability bin with width of 0.05. The length of each error stands for one standard deviation of all data within each variability bin. (Chu et al. 2013).

By hybridizing the two best ANN models for each season with an adaptive threshold scheme, a season-independent smart forecasting model is developed. Application of the smart model to an independent testing set shows that the proposed

smart forecasting methodology achieves the lowest mean absolute error during moderate variability periods, and its error distribution has the lowest bias, lowest standard deviation, and lowest occurrence of high absolute value errors among all forecasting models investigated. The combination of all these effects resulted in forecasting skills above the 20% level over persistence for five and ten minute forecast horizons.

### **5.3 Case Study: ISFM Using SkyCam**

In this case study, the ISFM integrates the smart forecasting engine with the SkyCam-based SACI cloud detection system. A size-adjustable grid-cloud-fraction method is applied to extract the numerical cloud indices ( $CI_i$ ) from the SkyCam image pre-processed by the SACI. The numerical  $CI_i$  are used as the inputs to the smart forecasting engine to predict one minute average global horizontal irradiance (GHI). Three months data of one-minute imaging and half-minute irradiance measurements collected in Folsom, California are used for model estimation and validation. The performance of the ISFM is assessed in terms of common error statistics (mean bias and root mean square error), but also in terms of forecasting skill over persistence.

High quality sky images and irradiance measurements are obtained using a Vivotek FE8171V SkyCam and a Rotating Shadowband Radiometer (Augustyn RSR-2, Manufactured by Irradiance, Inc), respectively. The RSR-2 is a first class radiometer that meets the requirements of accuracy. For both instruments, data are logged as 1 minute averages and are accessed in a MySQL database. Irradiance data and images are paired

and collected at 19920 time points during the winter and spring of 2013 (01/13/13 to 04/02/13). During these seasons there are sufficient data for different weather conditions. Data used for this study consider only periods when the solar elevation angle is larger than 30 degree. These data are randomly separated in two subsets: 70% as the learning set (14000 time points), and 30% as the testing set (5920 time points). The learning set is used to train and optimize the ISFM, and the testing set is used to assess the performance of the ISFM.

With the knowledge and experiences accumulated in the previous case study of ISFM with TSI. Improvements are made in the following aspects to further enhance the forecast performance of the ISFM:

1. Statistically enhanced image projection
2. Smoothed cloud motion detection
3. Size adjustable grid-cloud-fraction method
4. Training and testing data categorization
5. GA optimized ANN features (e.g. performance function)

The size-adjustable grid-cloud-fraction method is similar to the method developed by Marquez and C.F.M. Coimbra in 2013a. It can be summarized in four main steps: First, all images are projected from the convex mirror space onto a flat rectangular space (shown in Fig. 5.5 mid row) to remove the geometric distortion of the images. Then, pairs of consecutive images are processed using Particle Image Velocimetry (PIV) to compute

the flow direction of the clouds. The PIV algorithm (Mori and Chang (2003)) partitions the image into interrogation windows. The correlation between two consecutive interrogation windows is analyzed through the Minimum Quadratic Difference method (Mori and Chang (2003)) to determine the mean velocity of the clouds. After that, the SACI is employed to classify the sky images into binary cloud images. In the final step, a set of grid elements ( $X_1, X_2, \dots, X_6$ ) is placed over the binary cloud images originating from the position of the Sun and orienting in the reverse direction of the representative cloud velocity (shown in Fig. 5.5 bottom row). In this case study, the area of the GA-optimized grid elements is  $100 \times 100$  pixels. The cloud indices  $CI_i$  are calculated as the percentage of cloud pixels for the element  $i$ . This process is applied to all the images and  $CI_i$  time-series is generated as potential inputs to the ANN-based smart forecasting engine.

In addition the cloud indices, the total sky cloudiness and the time-lagged measured GHI values, ranging from 0 to 20 minutes in steps of 5 minutes are considered as potential inputs.

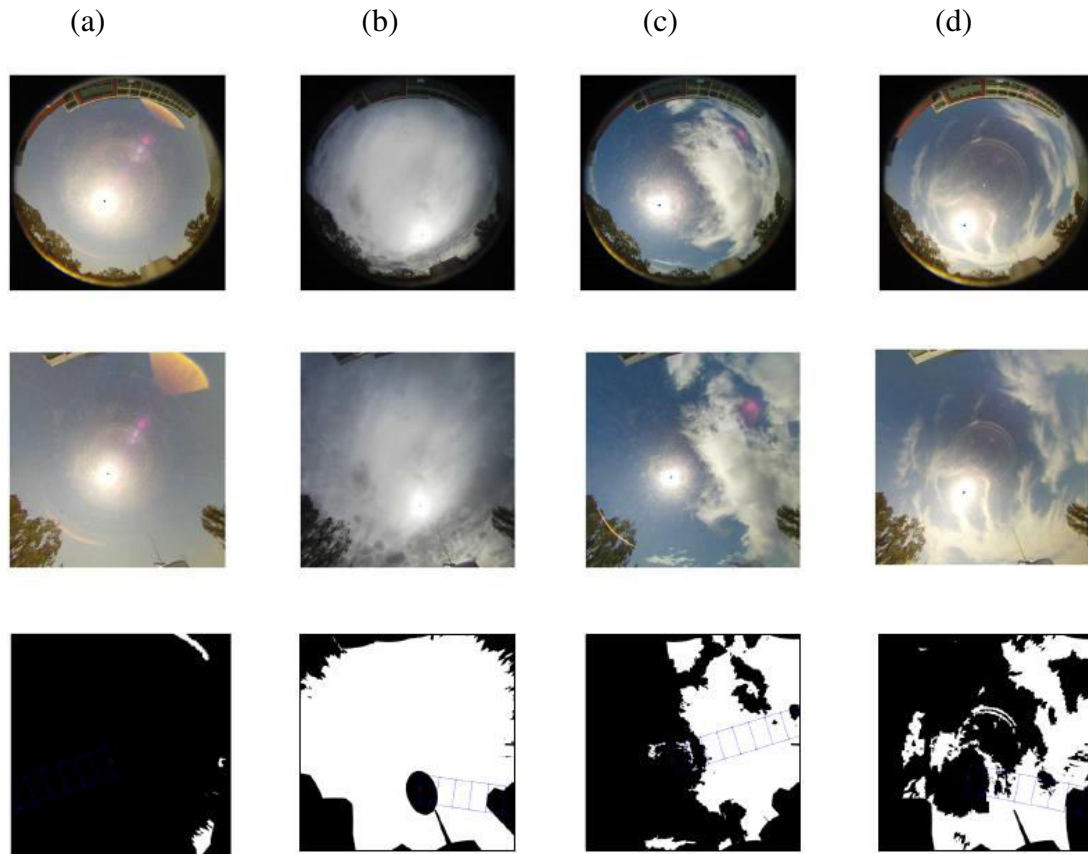


**Figure 5.5** Examples of SACI cloud identification for the Folsom SkyCam for (a) clear, (b) overcast, and (c) partly cloudy with optically thick clouds, and (d) optically thin clouds sky images. Top row presents the original images, middle row presents the projected images, and the bottom row presents the detected binary cloud maps with the grid elements. (Chu et al. 2015)

We use GAs to optimize the scheme for the ISFM. The optimizing process is same as discussed in Chapter 2.3.3 and 3.1. The GA optimization of the ANN-based forecasting engine takes 50 generations until the average fitness converges. The optimal set of input variables show that the total sky cloud coverage and cloud indices are useful for GHI forecast. The last measured values of GHI are selected as forecast inputs for all horizons. This indicates that the latest GHI values are highly informative for short term



irradiance forecast. The GA identifies that the optimal ANN scheme of ISFM consists of 1 hidden layer and 7 neurons per layer.

The GA optimized ISFM are evaluated on the testing set that is independent of the training process. The forecasting performance metrics are presented in Table 5.3 and are compared to that of the persistence model. In terms of bias, both persistence and ISFM exhibit small values. In terms of RMSE and forecast skill, the ISFM significantly outperforms the persistence. The results show that ISFM benefits from integrating the cloud cover information achieving forecast skills from 14.4% to 19.7% against the persistence model depending on the forecast horizon.

To further understand the performances of the ISFM, its error distributions for the 5-, 10- and 15-min horizons are plotted in Fig. 5.6. These figures show that, in the low error region (between  $-0.1$  and  $0.1 \text{ kW m}^{-2}$ ), both persistence and ISFM have sharp peaks near the 0. However, the persistence forecast has a higher frequency of errors with high absolute values ( $> 0.2 \text{ kW m}^{-2}$ ) resulting in a longer and heavier tail of error distribution. Compared to the persistence model, the ISFM reduces the occurrence of high absolute value errors, particularly for negative errors, and produces an error distribution with shorter tails and rounder shoulders. Consequently, the distributions of ISFM forecast errors are narrower, resulting in lower RMSEs and higher forecast skills.

**Table 5.2** Statistical error metrics for testing results of the different forecast models for 5, 10, and 15 minutes horizons. MBE and RMSE are in  $\text{Wm}^{-2}$ , s is in %.

	5 minute			10 minute			15 minute		
	MBE	RMSE	s	MBE	RMSE	s	MBE	RMSE	s
Persistence	0.9	90.6	0	-0.5	101.3	0	1.4	106.5	0
SkyCam-ISFM	2.3	77.5	14.4	-3	82.7	18.4	-0.4	85.5	19.7

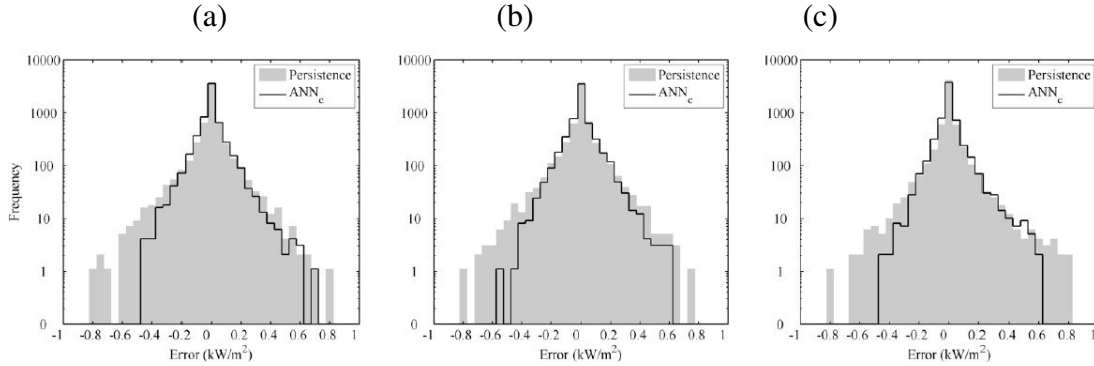


**Figure 5.6** Plots of error distributions for (a) 5 min, (b) 10 min, and (c) 15 min forecasts.  $\text{ANN}_c$  represents the ANN-based ISFM forecast using cloud-tracking techniques. The y-axis of the plots is in logarithmic scale. (Chu et al. 2013).

## 5.4 Summary

Integrated Solar Forecasting Model (ISFM), which integrates smart forecasting engine and ground-based sky-imaging system, is developed to predict one minute averaged values of both GHI and DNI for intra-hour horizons. Total sky imager (TSI) and SkyCam are used to capture sky images for the ISFM. A grid-cloud-fraction method is used to extract numerical cloud indexes from the sky images, and the ISFM takes the lagged measured irradiance and the cloud indexes as endogenous and exogenous inputs, respectively. The performance of the ISFM depends greatly on the selection of input variables. Also given that there are several parameters to be determined in the ANN-based smart forecasting engine (e.g. number of layers, number of neurons per

layer). GAs are employed to optimize all these free parameters. The results show that both TSI-based ISFM and SkyCam-based ISFM achieve forecasting skills around 20% over persistence model depending on forecast horizons. Compared to the sky imagers, the SkyCam have advantages such as substantially lower cost, higher spatial resolution, portability, and ease of installation. Therefore, SkyCam is selected as the sky imaging system for ISFM.

This work represents a significant improvement of intra-hour solar forecasting by developing a novel smart forecast model through the integration of advanced stochastic learning methods with sky imaging techniques.

### **Acknowledgements**

Chapter 5, in part, is a reprint of the publications: Y. Chu, H.T.C. Pedro, and C.F.M. Coimbra (2013) “Hybrid Intra-Hour DNI Forecasts with Sky Image Processing Enhanced by Stochastic Learning”, *Solar Energy* (98) pp. 592-603; and Y. Chu, H.T.C. Pedro, M. Li, and C.F.M. Coimbra (2015) “Real-Time Forecasting of GHI and DNI Solar Ramps with Smart Image Processing”, *Solar Energy* (114) pp. 91-104. The dissertation author was the first author of these papers.

## 6 Prediction Intervals for ISFM

### 6.1 Methods

A Hybrid model is developed to estimate prediction intervals (PIs) for the ISFM. The combination of the proposed Hybrid model with the ISFM is denoted as Hybrid-ISFM. This Hybrid model, which integrates sky imaging techniques, Support Vector Machine (SVM), and ANNs, is developed using high-quality irradiance and imaging measurements. The inputs to this Hybrid model are lagged time series of numerical local-sensing information, direct normal irradiance (DNI), and diffuse irradiance (DIF). The Hybrid model first uses a SVM to classify the current time series of irradiance into two categories: low variability period (lv) and high variability period (hv). Then PIs are generated by  $ANN_{lv}$  or  $ANN_{hv}$ , which are trained with data collected in lv and hv periods respectively.

Cloud cover directly affects the level of irradiance at ground. Therefore, sky images that provide information of cloud cover are useful to the Hybrid model. SkyCam images are recorded and stored as 8-bit RGB images. Generally, cloud pixels have a higher red (R) intensity values than sky pixels. Therefore, the normalized ratio ( $NRBR=(R-B)/(R+B)$ ) of the red intensity to the blue intensity are useful to identify the presence of clouds from images (exemplified in Fig. 6.1). NRBR shows improved robustness because it avoids extremely large value when pixels have very low blue intensities (Li et al. (2011), Chu et al. (2014)).

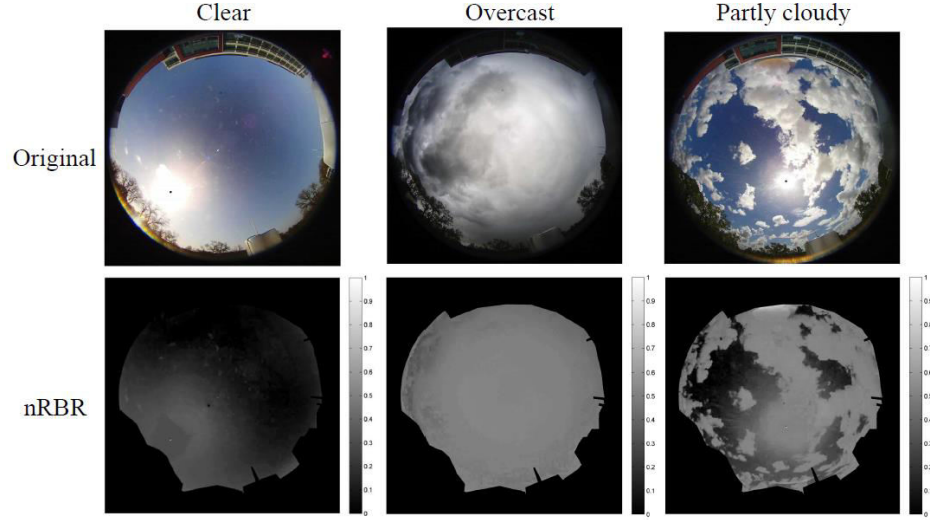


**Figure 6.1** Examples of original images (top row) and normalized RBR (NRBR) images (bottom row) for clear period (left column), overcast period (mid column), and partly cloudy (right column) period. The grey scales indicate the NRBR magnitudes in each image. (Chu et al. 2015).

NRBR are used to extract numerical metrics from the SkyCam images. Three metrics for a sky image are calculated: mean, standard deviation and entropy.

Mean:

$$\mu = \frac{1}{N} \sum_{i=1}^N \text{nRBR}_i, \quad (6.1)$$

where  $N$  is the number of pixels.

Standard Deviation:

$$\sigma = \sqrt{\frac{1}{N} \sum_{i=1}^N (\text{nRBR}_i - \mu)^2}. \quad (6.2)$$

Entropy

$$e = - \sum_{j=1}^{N_B} p_j \log_2(p_j), \quad (6.3)$$

where  $p_j$  is the relative frequency for the  $j^{\text{th}}$  bin ( $N_B=256$  bins evenly spaced).

The  $\mu$ ,  $\sigma$ , and  $e$  are used as inputs to the Hybrid model. In addition to the three image-related inputs (Eq. 6.1-6.3), time-lagged DNI and DIF measurements (ranging

from 0 to 20 min in steps of 5 min) is also considered as inputs because: 1) latest measured DNI are highly informative for intra-hour forecasts of DNI (Chu et al. (2013)). 2) Significant variation of DIF usually associates with cloud enhancement when clouds are close to the solar disk and therefore is an indicator of possible ramp events in future (Yordanov et al. (2013)).

The Hybrid model generates PIs using ANNs that are trained with the similar process as the Bootstrap method. The Bootstrap method is frequently used to generate PIs for ANN point forecasts due to its simplicity and ease to implement (Carney et al. (1999), Khosravi et al. (2011), Khosravi et al. (2013)). The key steps of the Bootstrap method are presented as followed:

The Bootstrap method for ANN forecasts (denoted as Bootstrap-ANN) first randomly sampling the training set with replacement to obtain N bootstrap re-sampled sets (N is set to 200 as suggested in Khosravi et al. (2013)). Then each of these N re-sampled sets is used to train a bootstrap ANN, so N bootstrap ANNs are prepared. Predictions from all bootstrap ANNs are used to generate an ensemble prediction:

$$\hat{I}_f(t) = \left(\frac{1}{N}\right) \sum_{i=1}^N \hat{I}_i(t), \quad (6.4)$$

where subscript  $f$  represents the true regression (recall the Eq.1),  $\hat{I}_f(t)$  is the estimation of the true regression, and the variance of the N bootstrap predictions

$$\sigma_f^2(t) = \frac{1}{N} \sum_{i=1}^N (\hat{I}_i(t) - \hat{I}_f(t))^2, \quad (6.5)$$

is used to estimate the uncertainty of the true regression. The magnitude of the variance

square residuals ( $r$ ) at time  $t$  can be calculated as:

$$r^2(t) = \max\left\{\left(I(t) - \hat{I}_f(t)\right)^2 - \sigma_f^2(t), 0\right\}. \quad (6.6)$$

Using the same training data set  $M$ , a new ANN is trained to derive the mathematic relation between the input vector and the white noise  $\sigma_e$  through maximizing the log-likelihood of the residuals  $r$ :

$$\sigma_e = \operatorname{argmax} \sum_{i=1}^M \log\left(\frac{1}{\sqrt{2\pi\sigma_e^2(t_i)}} \exp\left(-\frac{r^2(t_i)}{2\sigma_e^2(t_i)}\right)\right), \quad (6.7)$$

where the subscript  $e$  represent the white noise in Eq.1 and the total uncertainty of  $\sigma$  is calculated using Bayesian estimation:

$$p\left(\hat{I}(t) \middle| \sigma(t)\right) = \int p(\hat{I}(t) | \sigma_e(t)) p(\hat{I}_f(t) | \sigma_f(t)) d(\hat{I}_f(t)). \quad (6.8)$$

Based on the assumption that errors are Gaussian distributed (Khosravi et al. (2013)), the posterior prediction  $\hat{I}(t) = \hat{I}_f(t)$  and the total variance  $\sigma^2(t) = \sigma_f^2(t) + \sigma_e^2(t)$ . PIs are calculated using the critical value  $z_{1-0.5a}$  of normal distribution:

$$\hat{I}(t) \pm z_{1-0.5a} \sigma(t), \quad (6.9)$$

where  $1-0.5a$  is the nominal confidence interval.

The Bootstrap-ANN model uses 200 ANNs to predict the true regression and 1 ANN to predict the noise. Therefore, in total 201 ANNs is needed and requires enormous computational effort, which is a main drawback for this method because computational cost is a major concern for intra-hour forecasts in real-time.

The Hybrid model is developed using the followed steps: The training set can be categorized into two distinct phases (Chu et al. (2013), Chu et al. (2014)): the low

variability period (lv), defined as  $(I(t+\Delta t) - I(t))/I_{\text{clr}}(t) < 0.05$ , and the high variability period (hv), defined as  $(I(t+\Delta t) - I(t))/I_{\text{clr}}(t) > 0.05$ . lv is usually associated with clear or overcast sky conditions and hv is usually associated with partly cloudy sky conditions. Therefore, the training set can be labeled and divided into a lv subset and a hv subset.

Two ANN schemes ( $\text{ANN}_{\text{lv}}$  and  $\text{ANN}_{\text{hv}}$ ) are trained using the lv subset and the hv subset, respectively. To reduce the computational cost and to simplify the Hybrid model for real time forecasting, both  $\text{ANN}_{\text{lv}}$  and  $\text{ANN}_{\text{hv}}$  are trained to directly predict the Hybrid forecast  $\hat{I}_f(t)$  and associated total uncertainty  $\sigma(t)$  without considering the uncertainty of the true regression. Each of the two ANN schemes needs only 2 ANNs: 1 for predicting  $\hat{I}_f(t)$  and 1 for predicting the  $\sigma(t)$ . The ANN for modeling  $\sigma(t)$  is trained using the same maximum likelihood estimation method discussed in Eq. 6.7 by maximizing the log-likelihood of Hybrid forecast residuals  $r^2(t) = (I(t) - \hat{I}_f(t))^2$ .

For the proposed Hybrid model, a SVM is first trained using the whole training set to perform the classification of the DNI variability level (0 for lv and 1 for hv). We define a reference persistence classifier to benchmark the performance of the SVM classifier. This persistence classifier assumes the DNI variability level remains the same within the forecast horizon. The trained SVM and two ANN schemes are used to create the Hybrid model, which is defined as:

$$\{\hat{I}(t + \Delta t), \sigma(t + \Delta t)\} = \begin{cases} \text{ANN}_{\text{lv}}(t) & \text{if } \text{SVM}(t) = 0 \text{ (lv)} \\ \text{ANN}_{\text{hv}}(t) & \text{if } \text{SVM}(t) = 1 \text{ (hv)} \end{cases} \quad (6.10)$$

where the SVM determines which ANN scheme to apply: when the SVM output is 0 (lv),



it applies  $\text{ANN}_{\text{lv}}$ , otherwise it applies  $\text{ANN}_{\text{hv}}$ . The selected ANN scheme predicts a Hybrid point forecast  $\hat{I}_f(t)$  and a Hybrid forecast variance  $\sigma(t)$ , and generates PIs using Eq 6.9.

Based on the ISFM, the Hybrid model consists of 1 SVM and only 4 ANNs. Therefore, the computational cost of the Hybrid model is substantially lower than the Bootstrap-ANN model and meets the computation time requirement for real-time applications. In addition, unlike the Bootstrap-ANN model, the Hybrid model does not modify the source algorithm (e.g. retraining the ANN) of the baseline forecasts.

Persistence PIs are used to benchmark the PIs from the Hybrid model. The uncertainty in the persistence forecast (Eq. 2.5) is estimated using the most recent persistence errors:

$$\sigma(t + \Delta t)^2 = \frac{1}{M} \sum_{i=0}^M (I(t - i) - \hat{I}_p(t - i))^2, \quad (6.11)$$

where  $M$  is the lagged time period, which is set to 1 hour empirically. Once the uncertainty  $\sigma$  is obtained, the persistence interval is generated using Eq. 6.9.

## 6.2 Case Study: Prediction Intervals for Intra-hour DNI Forecast

The Hybrid-ISFP integrates the Hybrid model with a SkyCam-based ISFM to predict the intra-hour PIs for one minute averaged DNI. The prediction horizons examined are 5, 10, 15, and 20 minutes. The Hybrid model is trained using one year of irradiance and imaging measurements and is validated using six-month of measured irradiance and sky image data. The proposed hybrid model is quantitatively assessed in

terms of three performance metrics: PI coverage probability (PICP), PI normalized average width (PINAW), and coverage width-based criterion (CWC) (discussed in Chapter 2.4). The validation performance of the Hybrid model is compared with that of two reference models: the persistence model and the Bootstrap-ANN model.

Irradiance data are collected using a Rotating Shadowband Radiometer (Augustyn RSR-2, Manufactured by Irradiance, Inc) installed at an observatory in Folsom, California (latitude =  $38.64^{\circ}$ , longitude =  $-121.14^{\circ}$ ). The RSR-2 simultaneously measures the DNI and DIF components of broadband solar irradiance every 30 seconds, and a Campbell Scientific CR1000 data logger is used to log the irradiance values. A SkyCam is installed next to the RSR-2 to collect 8-bit RGB sky images ( $1536 \times 1536$ ). This SkyCam uses a 3.1MP CMOS sensor and a 360 degree panoramic view lens. The captured sky images are transferred (via FTP) to a remote server every minute. The irradiance data and the sky images are stored in a MySQL database.

Irradiance values and images are paired as data points. One year (January 13, 2013 to Dec 31, 2013) of historical data are assigned as the training set for model training. Six months (January 1, 2014 to June 11, 2014) of historical data are assigned as the validation set for model validation. Both the training and validation sets include the possible range of irradiance variability caused by diverse weather conditions.

Data quality is essential for the robustness and accuracy of the forecasts. The RSR-2 is a first-class radiometer that meets the accuracy requirements of our study. A

Licor LI-200 pyranometer is employed in the same location to provide redundant irradiance measurements for data quality control. The fish-eye lens is regularly cleaned to maintain the quality of sky images, and sky images with excessive amount of dust are manually removed from the database. During low Sun elevation period, ground obstacles (e.g. trees) adversely affect the accuracy of irradiance measurements. Therefore, the employed forecasts only consider data points collected during periods when the solar elevation angle is higher than  $15^\circ$ .

Prediction intervals of persistence, Bootstrap-ANN and Hybrid models are generated for four nominal confidence levels (68.3%, 80%, 90%, and 95%) and are assessed on the validation set. The validation results are presented in Fig. 6.2 and Table. 6.1. Ideally, PIs should have high PICP and low PINAW indicating high coverage probability of target values and high informativeness, respectively. At the same confidence level, the PIs generated by the Hybrid model mostly have higher PICPs and PINAWs than the PIs generated by the persistence and Bootstrap-ANN models. At the same confidence level, the PIs generated by the Hybrid model usually have higher PICPs and PINAWs than the PIs generated by the persistence and Bootstrap-ANN models (shown in Fig. 6.2a). Therefore in the Fig. 6.2b, Hybrid markers achieve lower ratios of PINAW/PICP than persistence and Bootstrap-ANN markers.

PIs are considered as ‘valid’ if their PICPs are greater than their nominal confidence level. For instance, Hybrid PIs using 90% nominal confidence interval

achieve a PICP of 92.8% for 5-minute forecast on the validation set and therefore are considered as valid PIs. The Hybrid model is the only model that achieves PICPs mostly greater than their nominal confidence levels. PICPs of persistence and Bootstrap-ANN models are usually lower than their nominal confidence levels. As a result, CWCs of the Hybrid model are substantially lower than the CWCs of the other two models for various forecast horizons.

In addition, the CWCs of both persistence and Bootstrap-ANN models increase tremendously for hv period due to the decrease of PICPs during cloudy weather. This phenomenon is also observed in Khosravi et al. (2013). The Hybrid model, which applies specific forecasting scheme for different DNI variability levels, consistently achieves CWCs <10 for both lv and hv periods.

**Table 6.1** Results of CWCs for overall, low variability, and high variability periods on validation set. Boldface font identifies the best performance.

	Model	5-min	10-min	15-min	20-min
Overall	Persistence	6.57	18.89	40.97	86.63
	Bootstrap-ANN	2.39	13.25	21.78	54.40
	<b>Hybrid</b>	<b>0.24</b>	<b>0.27</b>	<b>0.28</b>	<b>0.29</b>
lv	Persistence	0.47	0.52	2.54	10.56
	Bootstrap-ANN	0.27	0.69	2.43	9.23
	<b>Hybrid</b>	<b>0.12</b>	<b>0.14</b>	<b>0.15</b>	<b>0.16</b>
hv	Persistence	393.52	660.92	955.92	1118.81
	Bootstrap-ANN	350.49	584.01	407.54	398.44
	<b>Hybrid</b>	<b>0.55</b>	<b>8.73</b>	<b>5.53</b>	<b>4.63</b>

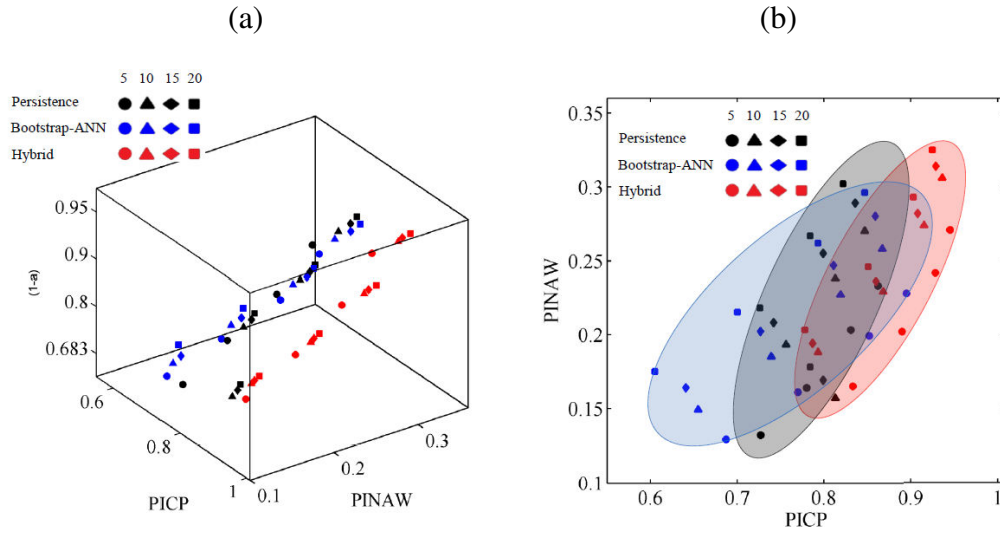


**Figure 6.2** (a) Forecast results of persistence, Bootstrap-ANN, and Hybrid models for various forecast horizons in 3-D space. X-axis represents PICP, y-axis represents PINAW, and z-axis represents the confidence level. (b) Plot of PINAWs with respect to PICPs. Each marker stands for one validation result that same to (a).

Sample time series of 10-minute horizon PI forecasts for persistence, Bootstrap-ANN, and Hybrid models are plotted in Fig. 6.3. During the lv periods (mostly clear and overcast as shown in Fig. 6.3.a and b), the PIs of all the three models achieve excellent coverage probability but different levels of informativeness. The persistence PIs achieve least average widths and therefore are most informative for lv periods. Bootstrap-ANN PIs have relatively broad widths because of its significant forecast residuals during lv periods, where the forecast residuals  $r^2$  are used as the training targets to estimate the uncertainty  $\sigma(t)$  (in Section 6.1). The point forecasts of the Bootstrap-ANN model has small negative bias for clear period and small positive bias for overcast period (Fig. 6.3a and b), and the above two kinds of forecast bias increase the magnitude of  $r^2$  and therefore increase the magnitude of  $\sigma$  for lv periods. The Hybrid

model first classifies the DNI variability level and then applies a specific ANN to forecast DNI. Therefore, the Hybrid model is more accurate than the Bootstrap-ANN in providing point forecasts for DNI during lv periods. As a result, the Hybrid PIs have very narrow widths achieving similar informativeness as the persistence PIs.

During the hv periods (mostly partly cloudy as shown in Fig. 6.3.c and d), accurate forecast of irradiance ramps is essential to the solar power plants for inverter control, plant management and real-time dispatch operations (Zhang et al. (2013)) (e.g. charging/discharging batteries, ancillary generation control). In period of ramp events, the Hybrid PIs covers most of the target values, achieving significantly higher PICPs than PIs from the persistence and Bootstrap-ANN models. The PIs generated by the persistence and Bootstrap-ANN models have low PICPs because their predictions of ramp events are usually subsequent in time to the true ramp events. With the SVM classifier, the PIs of the Hybrid model respond fastest to the changes of DNI variability level among the three models. This rapid response is useful to reduce the averaged PIs width while maintaining the high coverage probability.

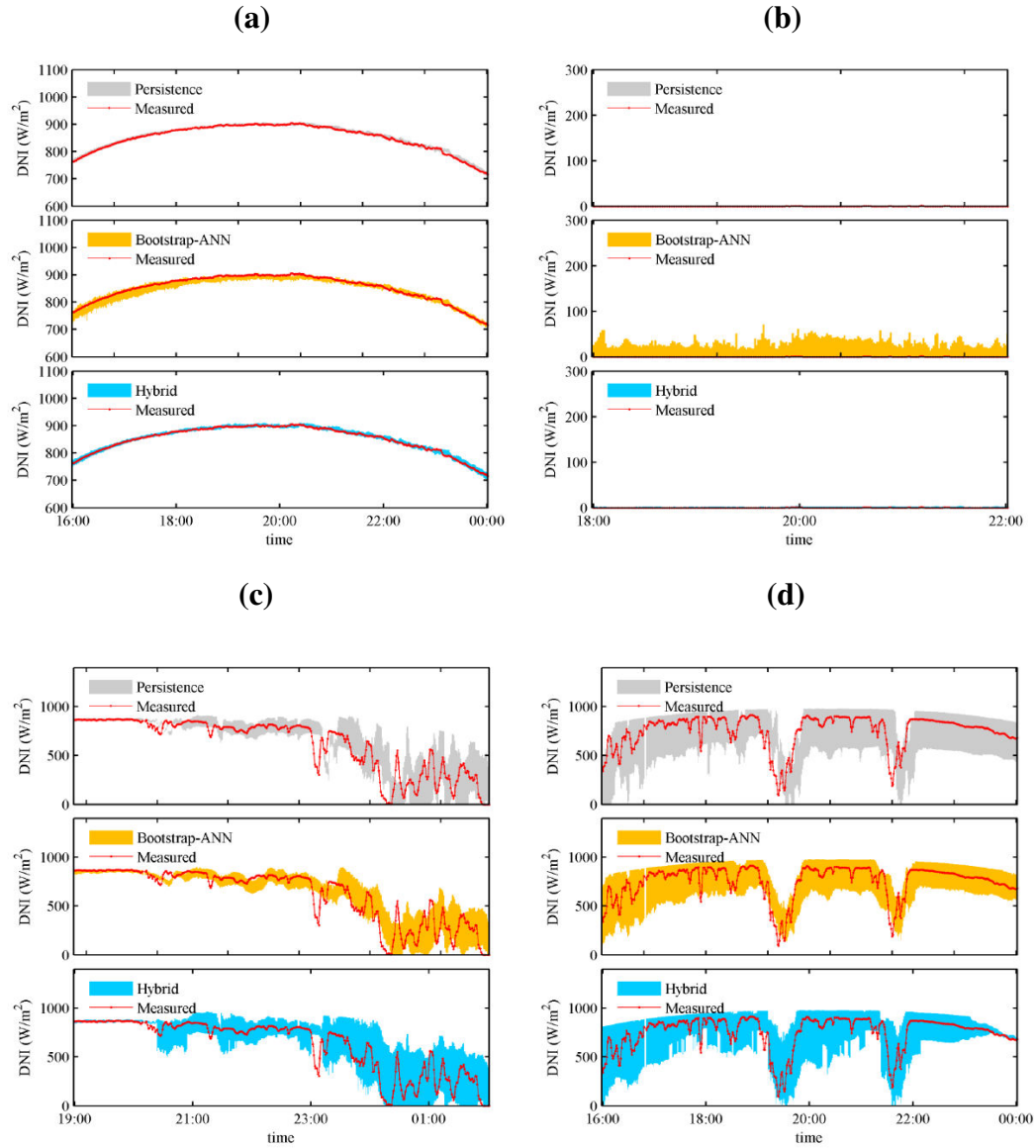


**Figure 6.3** Sample time series of 10-minute horizon PI forecasts for persistence, Bootstrap-ANN, and Hybrid models: a) clear period, b) overcast period, c) and d) partly cloudy period.

### 6.3 Case Study: Real Time Forecasting

A Hybrid-ISFM and a reference persistence model are deployed in real time at the same observatory in Folsom, CA to produce 5, 10, 15, and 20-minute PIs for DNI with a

confidence level of 90%. Both models have been mounting on our CPU servers at UCSD since July 1st, 2014 and operating every five minutes as unattended task when Sun elevation angle is larger than 15 degree. Results show that in real time the Hybrid-ISFM achieves coverage probabilities that are greater than the nominal 90%-confidence level regardless of forecast horizon and weather conditions.

The irradiance and sky image data for model training and real time forecasting are collected using the same devices and processed using the same method discussed in Chapter 6.3. One year (January 13, 2013 to Dec 31, 2013) of historical data are assigned as the training set for supervised model-training. The training set includes the possible range of DNI variability caused by diverse weather conditions. For the analysis, we monitor and analyze the persistence and the Hybrid-ISFM forecasts in real time from July 1, 2014 to September 23, 2014. The processing time to operate the forecasts for each time point is less than 5 seconds.

The classification accuracy of persistence and SVM classifiers are presented in Table 6.2, and the statistical results for the point forecasts are presented in Table 6.3. Hybrid point forecasts significantly outperform the reference persistence model and achieve forecast skills between 10% and 13% depends on forecast horizons.



**Table 6.2** Classification accuracy of DNI variability level in real time forecasting

	5-min	10-min	15-min	20-min
Persistence overall	0.89	0.87	0.86	0.85
Persistence for lv	0.92	0.91	0.91	0.91
Persistence for hv	0.78	0.68	0.64	0.60
SVM overall	0.91	0.87	0.87	0.86
SVM for lv	0.92	0.89	0.89	0.89
SVM for hv	0.86	0.85	0.83	0.82

**Table 6.3** Results for real-time point forecasts in terms of statistical metrics. MBE, MAE, and RMSE are in ( $\text{W/m}^2$ )

		5-min	10-min	15-min	20-min
Persistence	MBE	-0.4	-1.2	-2.2	-3.4
	MAE	37.5	45.8	53.4	58.6
	RMSE	102.6	124.3	139.0	149.1
	s	0.0%	0.0%	0.0%	0.0%
Hybrid	MBE	1.2	2.11	4.0	5.3
	MAE	35.7	44.2	51.8	56.8
	RMSE	93.1	111.5	122.3	131.8
	s	10.0%	10.3%	12.2%	11.6%

The performance of PIs is presented in Table 6.4. PIs are considered as invalid if their PICPs are less than their nominal confidence level (Khosravi et al. (2013)). In the real-time scenario, the Hybrid-ISFM achieves positive margins between PICPs and corresponding nominal confidence levels for both hv and lv periods. Therefore during the analyzed period, the PIs of the Hybrid-ISFM model are valid and reliable regardless of the variability level of DNI. The Hybrid-ISFM PIs are highly informative for lv periods and achieve low magnitudes of PINAWs. However, the PINAWs of Hybrid PIs are large

for hv period because of the highly variable nature of DNI particularly during the partly cloudy period.

**Table 6.4** Real time results of PICPs, PINAWs, and CWCs for overall, lv, and hv periods.

			5-min	10-min	15-min	20-min
Overall	PICP	Persistence	0.90	0.86	0.83	0.80
		Hybrid	0.97	0.95	0.96	0.95
	PINAW	Persistence	0.14	0.17	0.18	0.19
		Hybrid	0.22	0.24	0.28	0.30
	CWC	Persistence	0.32	1.25	6.90	32.27
		Hybrid	0.22	0.24	0.28	0.30
lv	PICP	Persistence	0.94	0.90	0.86	0.83
		Hybrid	0.98	0.97	0.98	0.98
	PINAW	Persistence	0.06	0.08	0.08	0.09
		Hybrid	0.11	0.11	0.15	0.17
	CWC	Persistence	0.06	0.08	0.57	3.09
		Hybrid	0.11	0.11	0.15	0.17
hv	PICP	Persistence	0.75	0.71	0.71	0.72
		Hybrid	0.92	0.92	0.92	0.91
	PINAW	Persistence	0.51	0.58	0.61	0.62
		Hybrid	0.71	0.81	0.82	0.83
	CWC	Persistence	75.02	779.91	816.41	547.37
		Hybrid	0.71	0.81	0.82	0.83

The persistence PICPs decrease significantly when forecast horizon increases, while Hybrid PICPs of different forecast horizons are in similar level. As we observed in Table 3, Hybrid point forecasts of longer horizons have larger errors than that of shorter horizons. Therefore, the forecast models of longer horizons are trained using larger forecast residuals and tend to predict larger uncertainty term and to generate PIs of

broader widths. The increase of uncertainties with respect to the increase of forecast horizons is also observed in Khosravi et al. (2013). With a relatively lower level of informativeness (overall < 8% higher in PINAW), the PIs of longer horizons achieve similar PICPs as PIs of shorter horizons.

Representative time series of 10-minute horizon forecasts are plotted in Fig. 3. During the lv periods (shown in Fig. 3.a and b), the PIs of both the persistence model and the Hybrid model achieve excellent coverage probability with high levels of informativeness. During the hv periods (shown in Fig. 3.c and d), the Hybrid PIs covers most of the target values achieving significantly higher PICPs than PIs from the persistence model. The PIs generated by the persistence have low PICPs because their predictions of ramp events are usually subsequent in time to the true ramp events. With the SVM classifier, the Hybrid model responds faster to the increase in DNI variability level (shown in Fig. 3.c) and achieves high coverage probability during ramp events. Accurate forecast of irradiance ramps is essential to solar power plants for inverter control, plant management and real-time dispatch operations (Zhang et al. (2013), Florita et al. (2013)). The Hybrid PIs provide possible ranges for the DNI ramps, quantify the uncertainty in the point predictions, and therefore provide useful information for plants or grid operators to make informed decisions to mitigate the weather-dependent variability of solar power production.

Example image of the monitor panel real time DNI PIs by the Hybrid-ISFM

model and cloud detection are illustrated in Fig. 6.5. This forecast is available at:

[http://132.239.222.136/PI\\_Folsom\\_Charlie/PI\\_realtime\\_Folsom.html](http://132.239.222.136/PI_Folsom_Charlie/PI_realtime_Folsom.html)

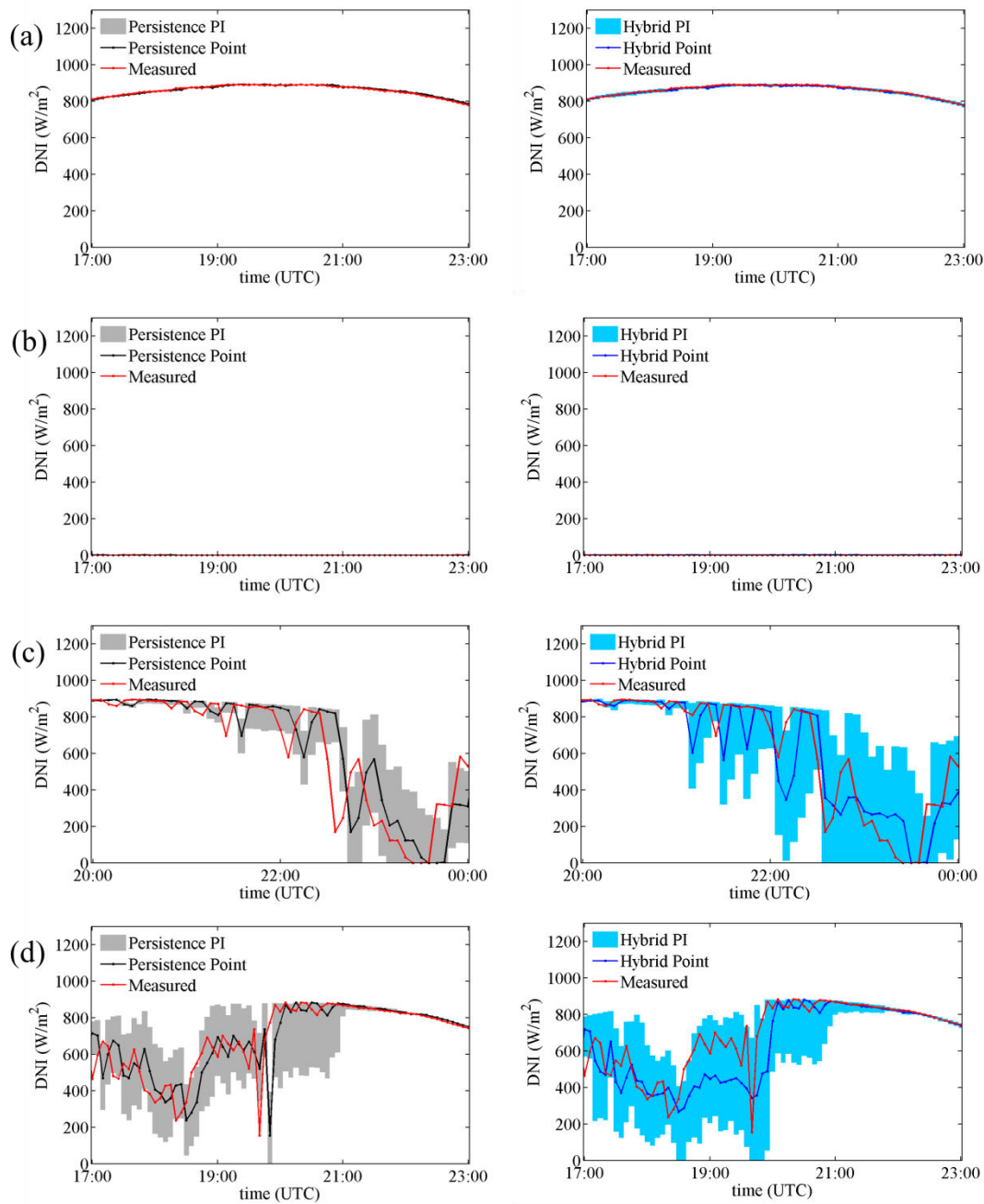


**Figure 6.4** Sample time series of 10-minute horizon forecasts from the persistence and the Hybrid models: (a) clear period, (b) overcast period, (c) and (d) partly cloudy period. (Chu et al. 2015).

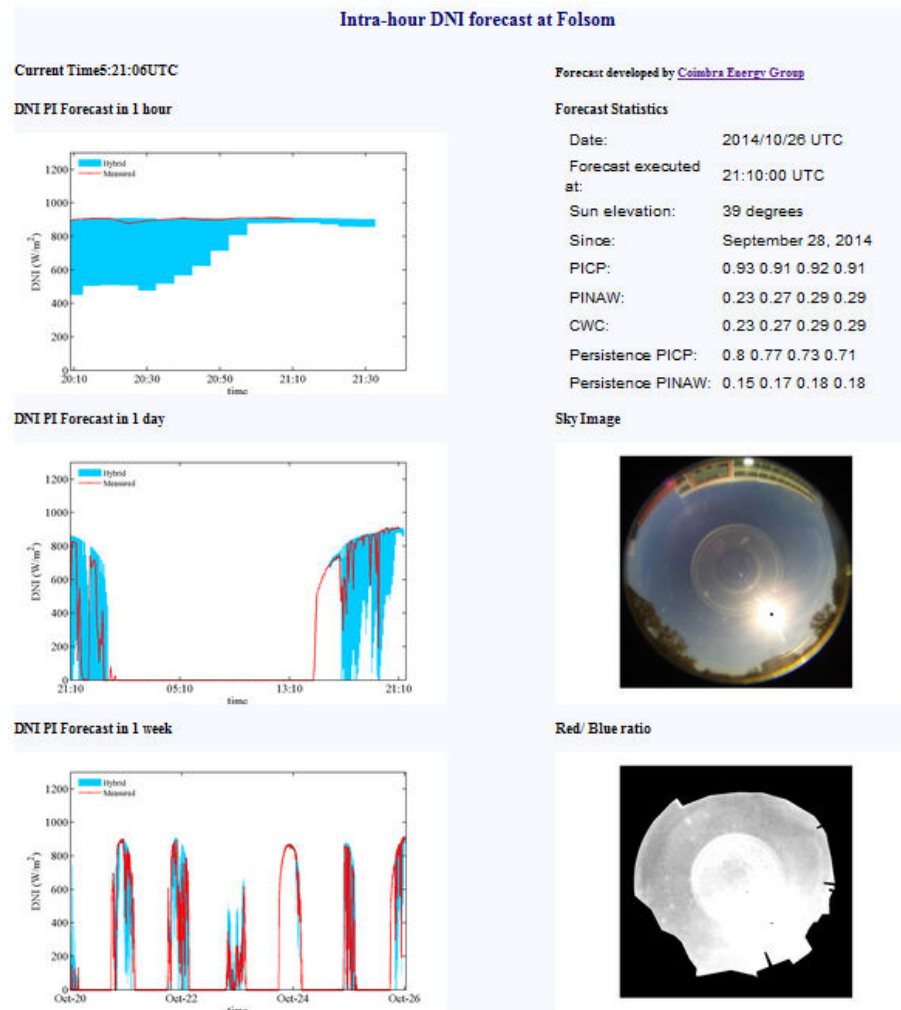


**Figure 6.5** Display of online real-time forecasting.

## 6.4 Summary

A Hybrid model is developed to generate real-time prediction intervals (PIs) for the ISFM. This proposed model integrates Support Vector Machine (SVM) algorithm, Artificial Neural Network (ANN) algorithm and sky-imaging techniques. The Hybrid model first uses a SVM classifier to categorize the present time into either low DNI variability period (lv) or high DNI variability period (hv). Then based on the categorized DNI variability level, the Hybrid model adaptively applies specific ANN schemes to

generate PIs for the ISFM point predictions.

In a case study at our observatory in Folsom, California, this Hybrid model is integrated with a SkyCam-based ISFM (Hybrid-ISFM) to generate PIs for intra-hour DNI. The Hybrid model is trained using 12-month irradiance and sky-image data and is validated using a six-month validation data set. Persistence model and Bootstrap-ANN model are employed as the reference models to benchmark the Hybrid model. The PIs generated from the three models are quantitatively assessed in terms of three metrics: PI coverage probability (PICP), PI normalized average width (PINAW), and coverage width-based criterion (CWC). The results show that at similar level of PINAW, the Hybrid-ISFM substantially outperforms the reference models in term of PICP and CWC regardless of the forecast horizon and the level of DNI variability. In addition, the Hybrid PIs respond rapidly to the changes of DNI variability level and achieve high coverage probability during ramp events.

When applied in real time, the PIs from the Hybrid-ISFM successfully quantify the uncertainty of point predictions, provide possible range for the target DNIs, achieve coverage probabilities which are mostly higher than the nominal confidence levels, and therefore provide highly relevant information that is potential to mitigate the variability of solar power productions.

## **Acknowledgements**

Chapter 6, in part, is a reprint of the publication: Y. Chu, M. Li, H.T.C. Pedro, and C.F.M. Coimbra (2015) “Real-time Prediction Intervals for Intra-hour DNI Forecasts”, Renewable Energy (in press). The dissertation author was the first author of this paper.

## 7 Conclusions and Recommendations for Future Work

Most of the works in the literature to date are based on either the stochastic learning or ground-based sky imaging and provide point or time average forecasts. This work proposes a high-fidelity multilayered forecasting method (Hybrid-ISFM) to provide intra-hour prediction intervals (PIs) for broad-band solar irradiance. The successful development of the Hybrid-ISFM accomplishes four major achievements:

(1) A smart forecasting engine is developed based on ANN whose scheme is optimized using GAs. This forecasting engine is applied to power reforecast at a 48MW PV plant and significantly improves the performance of three baseline models (Det, ARMA, and kNN).

(2) A smart adaptive cloud identification (SACI) system is developed based on cost-competitive fish-eye Camera. This system is deployed to detect cloud cover for multiple locations in California and shows accuracies over 90% under multiple weathers.

(3) An integrated smart forecasting model (ISFM) is developed through integrating the smart forecast engine with the SACI. The ISFM is deployed to forecast GHI for our observatory in Folsom and achieves forecasting skills from 10% to 20% over the reference persistence model.

(4) A Hybrid model is developed to quantify the uncertainty of the ISFM. This Hybrid model is assembled with the ISFM (Hybrid-ISFM) in order to generate real-time PIs for solar irradiance. Since July 2014, the Hybrid-ISFM has been mounted on our CPU



server to produce real-time PIs for DNI in Folsom, CA and serves as a proof of concept for this novel forecast method. The Hybrid-ISFM significantly outperforms the reference persistence model and achieves coverage probabilities (91% to 94% depends on forecast horizon) that are greater than the nominal confidence level (90%) regardless of weather conditions.

The proposed Hybrid-ISFM provides more accurate and robust forecasts that are able to capture irradiance ramp. Successful deployments of the Hybrid-ISFM are highly potential to mitigate the intrinsic variability of solar power and to facilitate higher penetration levels of solar energy into the power grid. Additionally, this work represents a progress in the field of solar forecasts with accurate prediction intervals for the highly variable direct component of sunlight rather than the less variable, global counterpart whose forecasts have traditionally driven the field. The forecasting methodologies discussed in this dissertation are of increasing relevance for the southern California region as the number of both rooftop and solar farm installations continues to increase each year to meet the state's Renewable Portfolio Standards.

Future works include but not limited to: (1) Multifunctional reconfiguration of the Hybrid-ISFM for spatial forecasts of irradiance and utility power (e.g. Ivanpah CSP plant). Details of the Hybrid-ISFM will be refined according to the feedbacks from peer reviewers. (2) Dissemination of the Hybrid-ISFM through publication, national media, and application of Hybrid-ISFM for utility companies (e.g. SDG&E) to improve grid

security. (3) Integration of the Hybrid-ISFM with storage system or ancillary power system for smart generation control and energy dispatching.

## References

- Allmen, M., Kegelmeyer, W., 1997. The computation of Cloud-Base Height from paired whole sky imaging cameras. *Journal of Atmospheric and Oceanic Technology* 13 (1), 97-113.
- Bacher, P., Madsen, H., Nielsen, H. A., 2009. Online short-term solar power forecasting. *Solar Energy* 83 (10), 1772-1783.
- Bishop, C. M., 1994. Neural networks and their applications. *Review of Scientific Instruments* 65 (6), 1803-1832.
- Box, G. E., Jenkins, G. M., Reinsel, G. C., 2011. Time series analysis: forecasting and control. Wiley 734.
- Brockwell, P. J., Davis, R. A., 2002. Introduction to time series and forecasting. Springer Verlag.
- Cao, J., Lin, X., 2008. Study of hourly and daily solar irradiation forecast using diagonal recurrent wavelet neural networks. *Energy Conversion and Management* 49, 1396–1406.
- CAISO., 2010. Integration of Renewable Resources - Operational Requirements and Generation Fleet Capability at 20% RPS. Technical report, August, 2010; Available at <http://www.caiso.com/2804/2804d036401f0.pdf>.
- Calbo, J., Sabburg, J., 2008. Feature extraction from whole-sky ground-based images for cloud-type recognition. *Journal of Atmospheric and Oceanic Technology* 25, 3-14.
- Carney, J.G., Cunningham, P., Bhagwan, U., 1999. Confidence and prediction intervals for neural network ensembles, in: Neural Networks, 1999. IJCNN'99. International Joint Conference on, IEEE. pp. 1215–8.
- Carter, G. M., Dallavalle, J. P., Glahn, H. R., 1989. Statistical forecasts based on the National Meteorological Center's numerical weather prediction system. *Weather and Forecasting* 4 (3), 401-412.
- Cazorla, A., Olmo, F. J., Alados-Arboledas, L., 2008. Development of a sky imager for cloud cover assessment. *JOSA A* 25, 29-39.

- Chang, C., Lin, C., 2011. LIBSVM: A library for support vector machines. *ACM Transactions on Intelligent Systems and Technology* 2, 27:1–27:27.
- Chow, C. W., Urquhart, B., Lave, M., Dominguez, A., Kleissl, J., Shields, J., Washom, B., 2011. Intra-hour forecasting with a total sky imager at the UC San Diego solar energy testbed. *Solar Energy* 85(11), 2881–2893.
- Chu, Y., Pedro, H., Coimbra, C.F.M., 2013. Hybrid intra-hour DNI forecasts with sky image processing enhanced by stochastic learning. *Solar Energy* 98, 592–603.
- Chu, Y., Pedro, H., Nonnenmacher, L., Inman, R.H., Liao, Z., Coimbra, C.F.M., 2014. A smart image-based cloud detection system for intra-hour solar irradiance forecasts. *Journal of Atmospheric and Oceanic Technology* 31(9) 1995–2007.
- Chu, Y., Urquhart, B., Gohari, S.M.I., Pedro, H.T.C., Kleissl, J., and Coimbra, C.F.M., 2015. Short-term reforecasting of power output from a 48 MWe solar PV plant. *Solar Energy* 112, 68-77.
- Chu, Y., Pedro, H.T.C., Li, M., and Coimbra, C.F.M., 2015. Real-time forecasting of solar irradiance ramps with smart image processing. *Solar Energy* 114, 91-104.
- Chu, Y., Li, M., Pedro, H.T.C., and Coimbra, C.F.M., 2015, Real-time prediction intervals for intra-hour DNI forecasts. *Renewable Energy*, in press.
- Crispim, E. M., Ferreira, P. M., Ruano, A. E., 2008. Prediction of the solar radiation evolution using computational intelligence techniques and cloudiness indices. *International Journal of Innovative Computing, Information and Control* 4(5), 1121–1133.
- Elizondo, D., Hoogenboom, G., McClendon, R. W., 1994. Development of a neural network model to predict daily solar radiation. *Agricultural and Forest Meteorology* 71(1), 115–132.
- Federal Energy Regulatory Commission & North American Electric Reliability Corporation., 2012. Arizona-Southern California Outages on September 8, 2011. Available at: <http://www.ferc.gov/legal/staff-reports/04-27-2012-ferc-nerc-report.pdf>
- Ghonima, M. S., Urquhart, B., Chow, C. W., Shields, J. E., Cazorla, A., Kleissl, J., 2012. A method for cloud detection and opacity classification based on ground based

- sky imagery. *Atmospheric Measurement Techniques Discussions* 5(4), 4535-4569.
- Hammer, A., Heinemann, D., Lorenz, E., Lucke, B., 1999. Short term forecasting of solar radiation: a statistical approach using satellite data. *Solar Energy* 67, 139–150.
- Hamill, T. M., Whitaker, J. S., Wei, X., 2004. Ensemble reforecasting: Improving medium-range forecast skill using retrospective forecasts. *Monthly Weather Review* 132 (6), 1434-1447.
- Hamill, T. M., Whitaker, J. S., Mullen, S. L., 2006. Reforecasts: An important dataset for improving weather predictions. *Bulletin of the American Meteorological Society* 87 (1), 33-46.
- Hassanzadeh, M., Etezadi-Amoli, M., Fadali, M. S., 2010: Practical approach for sub-hourly and hourly prediction of PV power output. In *North American Power Symposium (NAPS)*, 1-5.
- Heinle, A., Macke, A., and Srivastav, A., 2010. Automatic cloud classification of whole sky images. *Atmos. Meas. Tech.* 3, 557-567.
- Heskes, T., 1997. Practical confidence and prediction intervals. *Advances in neural information processing systems* 9, 176–182.
- Hiyama, T., Kitabayashi, K., 1997. Neural network based estimation of maximum power generation from PV module using environmental information. *Energy Conversion, IEEE Transactions on* 12 (3), 241-247.
- Holland, J. H., 1975. *Adaptation in natural and artificial systems: An introductory analysis with applications to biology, control, and artificial intelligence*. U Michigan Press, Ann Arbor, MI.
- Holland, J. H., 1992. *Adaptation in natural and artificial systems: an introductory analysis with applications to biology, control and artificial intelligence*. MIT press.
- Huang, Y., Lu, J., Liu, C., Xu, X., Wang, W., Zhou, X., 2010. Comparative study of power forecasting methods for PV stations. In *Power System Technology (POWERCON), 2010 International Conference, IEEE*. 1-6.

- Johnson, R. W., Hering, W. S., and Shields, J. E., 1989. Automated Visibility & Cloud Cover Measurements with a Solid State Imaging System. Marine Physical Laboratory, Scripps Institution of Oceanography, DTIS (Stinet) File ADA216906, University of California, San Diego.
- Johnson, R. W., Koehler, T. L., and Shields, J. E., 1988. A multi-station set of whole sky imagers and a preliminary assessment of the emerging data base. In Proceedings of the Cloud Impacts on DOD Operations and Systems, 1988 Workshop (Science and Technology Corporation, 1988), 159-162.
- Kalnay, E., Kanamitsu, M., Kistler, R., Collins, W., Deaven, D., Gandin, L., Joseph, D., 1996. The NCEP/NCAR 40-year reanalysis project. *Bulletin of the American Meteorological Society* 77 (3), 437-471.
- Kalogirou, S. A., 2001. Artificial neural networks in renewable energy systems applications: a review. *Renewable and sustainable energy reviews* 5 (4), 373-401.
- Khosravi, A., Nahavandi, S., Creighton, D., 2013. Prediction intervals for short-term wind farm power generation forecasts. *Sustainable Energy, IEEE Transactions on* 4 (3), 602–610.
- Khosravi, A., Nahavandi, S., Creighton, D., Atiya, A.F., 2011. Lower upper bound estimation method for construction of neural network-based prediction intervals. *Neural Networks, IEEE Transactions on* 22, 337–346.
- Koehler, T. L., Johnson, R. W., and Shields, J. E., 1991. Status of the whole sky imager database. In Proceedings of the Cloud Impacts on DOD Operations and Systems, 1991 Conference (Phillips Laboratory, Directorate of Geophysics, Air Force Materiel Command, Hanscom Air Force Base, 1991), 77-80.
- Kohavi, R., 1995. A study of cross-validation and bootstrap for accuracy estimation and model selection. *International Joint Conference on Artificial Intelligence* 14, 1137–1145.
- Krishnamurti, T. N., Kishtawal, C. M., LaRow, T. E., Bachiochi, D. R., Zhang, Z., Williford, C. E., Surendran, S., 1999. Improved weather and seasonal climate forecasts from multimodel superensemble. *Science* 285 (5433), 1548-1550.
- Lave, M., Kleissl, J., Stein, J. S., 2012. A wavelet-based variability model (WVM) for solar PV power plants. *IEEE Transactions on Sustainable Energy* 4 (2), 501-509.

- Li, Q., Lu, W., Yang, J. 2011. A hybrid thresholding algorithm for cloud detection on ground-based color images. *Journal of Atmospheric and Oceanic Technology*, 28(10), 1286–1296.
- Li, C. H. and Lee, C. K., 1993. Minimum cross entropy thresholding. *Pattern Recognition* 26, 617-625.
- Li, C. H., and Tam, P. K. S., 1998. An iterative algorithm for minimum cross entropy thresholding. *Pattern Recognition Letters* 19, 771-776.
- Ineichen, P., 2008 A broadband simplified version of the Solis clear sky model. *Solar Energy* 82, 758-762.
- Ineichen, P. and R. Perez, 2002. A new airmass independent formulation for the Linke turbidity coefficient. *Solar Energy* 73 (3), 151-157.
- Long, C. N., and Ackerman, T. P., 2000. Identification of clear skies from broadband pyranometer measurements and calculation of downwelling shortwave cloud effects. *Journal of Geophysical Research* 105, 15609-15626.
- Long, C. N., Sabburg, J. M., Calbó, J., and Pages, D., 2006. Retrieving cloud characteristics from ground-based daytime color all-sky images. *Journal of Atmospheric and Oceanic Technology* 23, 633-652.
- Lopez, G., Batlles, F.J., Tovar Pescador, J., 2005. Selection of input parameters to model direct solar irradiance by using artificial neural networks. *Energy* 30, 1675–1684
- Marquez, R., Coimbra, C.F.M. 2011. Forecasting of global and direct solar irradiance using stochastic learning methods, ground experiments and the NWS database. *Solar Energy* 85(5), 746–756.
- Marquez, R., Gueorguiev, V., Coimbra, C. F. M., 2013. Forecasting of Global Horizontal Irradiance Using Sky Cover Indices, *ASME Journal of Solar Energy Engineering* 135, 0110171-0110175.
- Marquez, R. Coimbra, C.F.M., 2013a. Intra-hour DNI forecasting based on cloud tracking image analysis. *Solar Energy* 91, 327-336.

- Marquez, R. & Coimbra, C.F.M. 2013b. Proposed metric for evaluation of solar forecasting models. *ASME Journal of Solar Energy Modeling* 135, 0110161-0110169.
- Marquez, R., Pedro, H. T. C., Coimbra, C. F. M., 2013. Hybrid Solar Forecasting Method Uses Satellite Imaging and Ground Telemetry as Inputs to ANNs. *Solar Energy* 92, 172-188.
- Melgani, F., Bruzzone, L., 2004. Classification of hyperspectral remote sensing images with support vector machines. *Geoscience and Remote Sensing, IEEE Transactions on* 42, 1778–90
- Mellit, A., Kalogirou, S. A., 2008. Artificial intelligence techniques for photovoltaic applications: A review. *Progress in Energy and Combustion Science* 34(5), 574–632.
- Mellit, A., Pavan, A. M., 2010. A 24-h forecast of solar irradiance using artificial neural network: Application for performance prediction of a grid connected PV plant at Trieste, Italy. *Solar Energy* 84, 807–821.
- NREL. (2010). WWSIS: Western Wind and Solar Integration Study. Technical Report, May 2010; Available at <http://www.nrel.gov/wind/systemsintegration/wwsis.html>.
- Paoli, C., Voyant C., Muselli M., Nivet M.L., 2010. Forecasting of Preprocessed Daily Solar Radiation Time Series Using Neural Networks. *Solar Energy* 84 (12), 2146-2160.
- Pedro H.T.C., Coimbra, C.F.M., 2012. Assessment of Forecasting Techniques for Solar Power Output with No Exogenous Inputs. *Solar Energy* 86, 2017-2028.
- Pinson, P., Nielsen, H.A., Møller, J.K., Madsen, H., Kariniotakis, G.N., 2007. Non-parametric probabilistic forecasts of wind power: required properties and evaluation. *Wind Energy* 10, 497–516.
- Reno, M. J., Hansen, C. W., and Stein, J. S., 2012. Global Horizontal Irradiance Clear Sky Models: Implementation and Analysis.
- Richards, K., Sullivan, G. D., 1992. Estimation of cloud cover using colour and texture. Springer London. In *BMVC92* ,436-442.



- Rossow, W. B., and Schiffer, R. A., 1991. ISCCP cloud data products. *Bulletin of the American Meteorological Society* 72, 2-20.
- Sfetsos, A., Coonick, A. H., 2000. Univariate and multivariate forecasting of hourly solar radiation with artificial intelligence techniques. *Solar Energy* 68, 169–178.
- Shields, J.E., Johnson, R.W., Koehler, T.L., 1993. Automated Whole Sky Imaging Systems for Cloud Field Assessment. *Proceedings of the Fourth Symposium on Global Change Studies*, Published by the American Meteorological Society, Boston MA, 17 – 22.
- Shields, J. E., Karr, M. E., Tooman, T. P., Sowle, D. H., Moore, S. T., 1998. The whole sky imager—a year of progress. In *Eighth Atmospheric Radiation Measurement (ARM) Science Team Meeting*, Tucson, Arizona, 23-27.
- Singh, G. K., 2013: Solar power generation by PV (photovoltaic) technology. A review. *Energy* 53, 1–13.
- Souza-Echer, M. P., Pereira, E. B., Bins, L. S., and Andrade, M. A. R., 2006. A simple method for the assessment of the cloud cover state in high-latitude regions by a ground-based digital camera. *Journal of Atmospheric and Oceanic Technology* 23, 437-447
- Urquhart, B., Chow, C.W., Nguyen, D., Kleissl, J., Sengupta, M., Blatchford, J., Jeon, D., 2012. Towards intra-hour solar forecasting using two sky imagers at a large solar power plant. *Proceedings of the American Solar Energy Society*, Denver, CO, USA, 2012.
- Voss, K., and Zibordi, G., 1989. Radiometric and geometric calibration of a visible spectral electro-optic 'fisheye' camera radiance distribution system. *Journal of Atmospheric and Oceanic Technology* 6, 652-662.
- Whitaker, J. S., Wei, X., Vitart, F., 2006. Improving week-2 forecasts with multimodel reforecast ensembles. *Monthly Weather Review* 134 (8), 2279-2284.
- Wilks, D. S., Hamill, T. M., 2007. Comparison of ensemble-MOS methods using GFS reforecasts. *Monthly Weather Review* 135 (6), 2379-2390.
- Yang, J, Lü, W., Ma, Y., Yao, W., and Li, Q., 2009. An Automatic Ground based Cloud Detection Method Based on Adaptive Threshold. *Journal of Applied*

Meteorological Science 20, 713-721.

- Ying-zi, L., Ru, L., Jin-cang, N., 2008. Forecast of power generation for grid-connected photovoltaic system based on grey model and Markov chain. ICIEA 2008 3rd IEEE Conference, 1729-1733.
- Yordanov, G.H., Midtgård, O., Sætre, T.O., Nielsen, H.K., Norum, L.E., 2013. Overirradiance (cloud enhancement) events at high latitudes. IEEE Journal of Photovoltaics 3, 271–277.
- Younes, S., and Muneer, T., 2007. Clear-sky classification procedures and models using a world-wide data-base. Applied Energy 84, 623-645.
- Zhang, J., Hodge, B., Florita, A., Lu, S., Hamann, H.F., Banunarayanan, V., 2013. Metrics for evaluating the accuracy of solar power forecasting. Technical Report. National Renewable Energy Laboratory, NREL/CP-5500-60142.
- Zhao, G., and Di Girolamo, L., 2006. Cloud fraction errors for trade wind cumuli from EOS-Terra instruments. Geophysical Research Letters 33(20).